Journal of Energy Storage 120 (2025) 116486

Contents lists available at ScienceDirect

Journal of Energy Storage

journal homepage: www.elsevier.com/locate/est

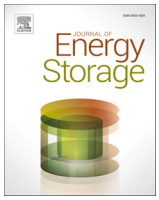

Research papers

Detailed investigation of degradation modes and mechanisms of a cylindrical high-energy Li-ion cell cycled at different temperatures

Christina Schmitt [a,*], Dennis Kopljar [a], K. Andreas Friedrich [a,b]

[a] Deutsches Zentrum für Luft- und Raumfahrt (DLR), Institute of Engineering Thermodynamics, 70569 Stuttgart, Germany
[b] University of Stuttgart, Institute of Building Energetics, Thermal Engineering and Energy Storage (IGTE), 70569 Stuttgart, Germany

ARTICLE INFO

Keywords:
Lithium ion battery
Battery degradation
Differential voltage analysis
Electrochemical impedance analysis
Post-mortem analysis

ABSTRACT

The temperature-dependent degradation of a cylindrical high-energy NCA/graphite-SiO_x cell is investigated by a combination of in situ and post-mortem techniques. Cells are cycled at 10 °C, 25 °C and 35 °C, with periodic check-up tests to identify the degradation modes during aging. Differential voltage analysis (DVA) identifies the primary degradation modes over all temperatures as the loss of the silicon active material as well as the loss of lithium inventory. Electrochemical impedance spectroscopy, evaluated by the distribution of relaxation times and equivalent circuit modeling, shows that the resistance increase is temperature dependent with a sudden increase after the sudden failure of the cells for all resistances except the cathode impedance, which is primarily cycle dependent. Notably, reversible Li plating is observed by differential open circuit voltage analysis in cells aged at 10 °C, despite moderate charging currents. The evaluation of the Coulombic efficiency shows the onset of irreversible Li plating coincides with the sudden failure of the cells. An extensive post-mortem analysis is conducted including SEM/EDS, XRD and electrochemical measurements in a three-electrode set-up. Post-mortem results reveal a more inhomogeneous degradation at lower temperatures compared to higher temperatures. In addition, it exposes the extent of the loss of the cathode active material at higher temperatures, which is masked in the DVA of the full cell. These results highlight the significant impact of temperature on battery performance and degradation mechanisms and show the benefit of post-mortem analysis in addition to non-invasive characterization techniques.

1. Introduction

The application of lithium ion batteries (LIBs) in electric vehicles (EVs) requires the combination of high energy density, safety, life-time, and performance. However, a high energy density in LIBs usually comes at the expense of power density and fast charging capabilities. To achieve a high acceptance of EVs by customers, the charging process of a battery should be as fast as possible while ensuring a long cycle life and safety. With increasing current rate, the (de)lithiation in high energy LIBs becomes more inhomogeneous, especially in the through-plane direction, due to transport limitations in the electrolyte of the porous electrodes [1]. In addition, the ohmic resistance of the cell might not be optimized for high current rates as a trade-off to increase the energy density, e.g. thin current collectors, fewer tabs, high coating thickness with less conductive additive. During charging, the resulting overpotentials could ultimately lead to the risk of Li plating on the anode side, which is a severe degradation mechanism and should be avoided at all costs. However, Li plating is only one of many degradation mechanisms such as solid electrolyte interphase (SEI) growth, particle cracking or transition metal dissolution [2–5].

Most of these mechanisms can only be identified by post-mortem analysis. However, they can be divided into different degradation modes that can be evaluated in situ by both differential voltage analysis (DVA) [6–9] and incremental capacity analysis (ICA) [10–12]. Non-invasive methods allow the observation of the cell degradation during aging and are therefore potentially suitable for real-time applications within a battery management system (BMS) to optimize the operation for a longer cycle life. The degradation mechanisms leading to capacity fade are often divided into loss of active material (LAM) and loss of lithium inventory (LLI) [2]. Typical degradation mechanisms resulting in LAM are particle cracking, binder decomposition, transition metal dissolution, structural disordering and graphite exfoliation. In contrast, LLI is mainly caused by SEI growth and Li plating [2]. However, differentiating the degradation of each active material in a cell with a

* Corresponding author.
E-mail address: Christina.Schmitt@dlr.de (C. Schmitt).

https://doi.org/10.1016/j.est.2025.116486
Received 29 October 2024; Received in revised form 10 March 2025; Accepted 30 March 2025

blend electrode, e.g. graphite and silicon on the anode side, can be challenging due to different degradation rates [8,13].

Another non-invasive method to evaluate the degradation modes is electrochemical impedance spectroscopy (EIS) [14,15]. EIS is applied to evaluate the conductivity loss (CL) [16,17], changes in internal electrochemical processes [18] and the influence of the degradation mechanisms on the performance [16]. The distribution of relaxation times (DRT) of full and half cells can be used to assign the processes observed in the full cell to the individual electrode [19–22], and can further be used to analyze the degradation modes [23–25].

However, non-invasive methods have their limits. To fully understand the mechanisms behind the degradation modes and validate non-invasive EIS and DVA predictions, opening the cell for post-mortem analysis is necessary. Waldmann et al. [3] provide a detailed review of the various methods that can be used to identify the underlying degradation mechanisms by post-mortem analysis. For this, the cells are opened after cycling to collect samples from the electrodes or separator for physical analysis such as scanning electron microscopy (SEM), energy dispersive spectrometry (EDS) or X-ray diffraction (XRD) [26–29]. In addition, electrochemical analysis of the harvested electrodes is useful, e.g. to measure the residual and the remaining capacity of the electrodes in half cells [3,29–32]. By combining both non-invasive testing and post-mortem analysis, more information about the accuracy of the in situ methods can be gained [26,33,34].

In this study, the degradation of a high-energy cylindrical cell with a graphite-SiO_x blend anode and a $LiNi_{0.87}Co_{0.11}Al_{0.02}O_2$ (NCA) cathode [1] is investigated by performing cyclic aging with regular check-up tests and post-mortem analysis. NCA is a common cathode material in LIBs due to its high specific capacity (up to 265 mAh g^{-1}) [35], outstanding cycle life, long-term storage capabilities and cost effectiveness [36]. NCA is superior than NMC materials with regard to electrolyte oxidation, transition metal dissolution and irreversible phase transitions [37]. However, NCA is prone to microcrack formation in the secondary particles, leading to a separation of the primary particles and particle pulverization. This results in an increased formation of the cathode electrolyte interface (CEI) and NiO on the surface of the primary particles [38,39]. Watanabe et al. [38,39] showed that this can be mitigated by reducing the depth of discharge (DoD).

To increase the energy density of the cell, up to 10 wt% SiO_x is added nowadays to the graphite anode in commercial cells [1]. However, SiO_x has a high volume change during cycling leading to continuous SEI formation, pulverization and loss of electrical contact, and thus, loss of cyclable Li as well as loss of active material [40,41]. By embedding SiO_x in a carbon matrix and/or mixing it with graphite, these degradation mechanisms can be mitigated [41]. However, tracking the degradation of a blend-electrode containing graphite and silicon is complex due to the different degradation mechanisms and rates of both active materials [8,42].

Several studies investigated the degradation of commercial cells [43–50] or self-made pouch cells [36,51] containing NCA as well as graphite-SiO_x. However, the influence of the temperature on the degradation of NCA/graphite-SiO_x cells is still unclear. The results from Watanabe et al. [38,39] suggest that temperature has only a minor influence on the degradation of NCA/graphite cells, especially with a maximum depth of discharge (DoD) of 60 %. In contrast, others showed that the temperature has a significant influence on the degradation of NCA/graphite-SiO_x cells [36,47,48,50].

This study aims to enhance the understanding on the temperature influence on the degradation of NCA/graphite-SiO_x cells by cycling cells under the same conditions at three different moderate temperatures. The degradation of the cells is evaluated by analyzing the cycling data and check-up tests using DVA, EIS and differential open circuit voltage (dOCV) to identify the primary degradation modes and differentiate observed degradation mechanisms. This approach is further validated by comparing the results with those obtained from post-mortem analysis showing how the different techniques complement each other in contributing to a thorough understanding of aging phenomena occurring under the specific cycling conditions. Importantly, we also aim to provide a comprehensive and detailed discussion on how to employ and interpret the results from various techniques commonly used to analyze degradation, yet rarely discussed in sufficient detail.

2. Experimental

2.1. Materials and methods

In this study, a commercial cylindrical 21700 cell (INR21700-50E) from Samsung with a nominal capacity of 4.9 Ah is investigated. The cell consists of a $LiNi_{0.87}Co_{0.11}Al_{0.02}O_2$ (NCA) cathode and a graphite-silicon composite anode [1] and was selected to serve as a representative example for a high energy density cylindrical cell with a blend anode. It is further fully parameterized in our previous publication [1] and can therefore serve as basis for the combination of continuum and degradation modeling. Important information from the datasheet can be found in Table S1.

2.2. Aging experiments

The cylindrical cells underwent cyclic aging at 10 °C, 25 °C and 35 °C with intermittent check-up tests at 25 °C. These aging temperatures were selected to represent typical operation temperatures of EVs in the range of moderate climate zones. The datasheet of the INR21700-50E cell does not include any recommendations for SoC or temperature dependent charge or discharge currents. Therefore, the cells were cycled at the manufacturer's maximum recommended charging rate of 0.5C from 0 % up to 80 % SoC. The upper SoC limit was set to 80 % SoC, consistent with fast charging protocols that use this threshold to minimize the overall charging time [52,53]. If the upper cut-off voltage of 4.2 V was reached before the 80 % SoC limit, the cell was charged with a subsequent constant current step until the 80 % SoC limit was reached by Coulomb counting. In the following discharge, the cell was discharged with 1C to 2.5 V. To evaluate the reproducibility, three cells were cycled at each temperature. Regular check-up tests were performed to keep track of the aging rate and behavior of the cell as shown in Fig. 1. The check-up test started with tempering the cell at 25 °C for at least 4 h, followed by three reference cycles consisting of a 0.5C constant-current constant-voltage (CC-CV) charge up to 4.2 V and a 1C constant current (CC) discharge to 2.5 V. The state-of-health (SoH) throughout cycling is based on the capacity of the second discharge step. In the last discharge

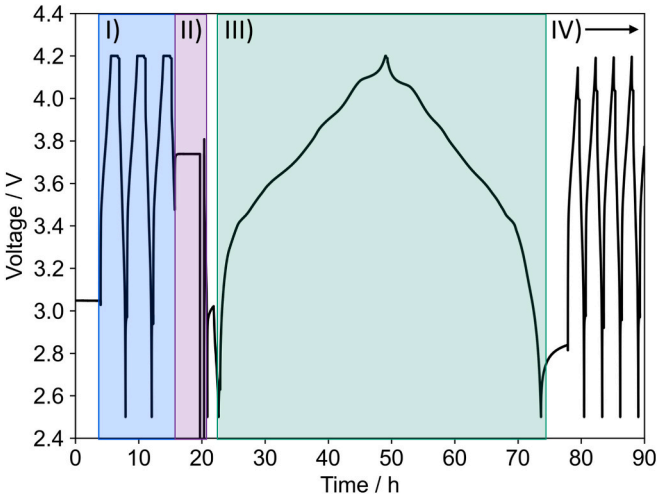

Fig. 1. Overview of test procedure: first check-up test with reference cycles (I), followed by EIS at 50 % SoC (II) and a pOCV cycle with C/25 (III). Then, the first cycles (IV) are shown (at 25 °C).

cycle, the cell is discharged to 50 % SoC of the previous discharge step by Coulomb counting, left to rest for 4 h to perform a galvanostatic impedance measurement from 3 kHz to 10 mHz with an amplitude of C/50. Afterwards, the cell was fully discharged before measuring a pseudo-OCV (pOCV) cycle with C/25 between 2.5 V and 4.2 V. Although the pOCV measurement is time-intensive, it allows to perform DVA over aging to identify the different aging modes over the life-time of the cells. After each check-up test, the charge capacity corresponding to 80 % SoC in the cycling protocol is adapted based on the capacity measured in the last check-up test. The tests were performed with a BaSyTec XCTS in Weiss WK340 climate chambers with automated temperature control. EIS were measured by a potentiostat from Zahner (Zennium Pro). In order to perform EIS during tests, a programmed Pi was connected to the BaSyTest software to automatically switch the electrical connection of the cell from the battery cycler to the potentiostat and back. Thus, highly accurate impedance measurements could be performed while being able to test and cycle several cells at the same time.

The software RelaxIS 3 (rhd instruments) [54] was used to analyze the impedance spectra by calculating the DRT of the spectra and by fitting of an equivalent circuit model (ECM) to the spectra. Both methods are applied to obtain the resistances of the different processes taking place in the battery cell. The calculation of the DRT in the software RelaxIS 3 is based on a discretization using a radial basis function followed by a fit to the experimental data using a Tikhonov regularization method. A second-order radial basis function derivative with a shape factor of 0.5 was applied with a Gaussian basis function using $\lambda = 0.0001$.

2.3. Post-mortem techniques

After the cells reached 80 % SoH or less, one cell from each temperature was investigated by post-mortem analysis. Following the last check-up test, the aged cells were transferred to the glove box for opening under argon atmosphere. To evaluate the degradation of the electrodes, a cell at begin-of-life (BoL) was also examined. The cells were opened in a discharged state at 0 % SoC for better comparability between cells and to evaluate the residual capacities of the electrodes. First, the cells were opened with a pipe cutter and then dismantled by a side cutter. Care was taken to avoid cross-contamination of both electrodes during their separation. At first, a visual inspection of the electrodes was performed before preparing samples for other tests.

2.3.1. SEM/EDS

The changes of the morphology of the electrode surface were observed by a scanning electron microscope (SEM) coupled with energy-dispersive X-ray spectroscopy (EDS). For this, the samples from the middle part of the sheet were washed twice for 1 min in dimethyl carbonate (DMC) before drying them for 30 min under vacuum to remove any salt or non-volatile solvent residues [3]. Due to a replacement of the SEM/EDS device at our institute, the BoL samples as well as the samples from the cells aged at 10 °C and 25 °C were measured with a Zeiss Gemini Ultra plus equipped with a Bruker XFlash detector 5010 whereas the samples from the cell aged at 35 °C were investigated with a Zeiss Crossbeam 350 equipped with an Oxford Ultim Max EDS detector.

2.3.2. XRD

The samples for X-ray diffractometry (XRD) are cut from representative positions of the electrode sheets and also washed twice for 1 min in DMC. An air-tight sample holder was used for measuring the different samples with a Bruker D8 Advance in Bragg-Brentano geometry. Rietveld refinement was performed with the software TOPAS (Bruker) to identify changes of crystal structure of the electrodes.

2.3.3. Electrochemical tests

The degradation of the electrodes was further evaluated by electrochemical tests. For this, the coating on one side of the bi-layered electrodes was removed as described in detail in Schmitt et al. [1] 18 mm discs were cut for tests with ECC-PAT-Core-Cells (EL-CELL) and then washed twice for 1 min in DMC. The cells were built in a three-electrode set-up with a Li reference ring (EL-CELL), Whatman GF/A separator and a Li counter electrode punched to 18 mm discs. 120 µl of 1 M $LiPF_6$ in a mixture of ethylene carbonate (EC) and DMC at a ratio of (1:1) vol% was used as electrolyte. For better readability, the term “half cell” is used below in relation to the three-electrode set-up.

After the cells were built, they were transferred to a Memmert IPP750 climate chamber operating at 25 °C and tested with a BaSyTec Cell Test System (CTS). First, the residual capacity of the NCA electrodes was measured by a C/25 discharge step (lithiation), while the residual capacity of the anode was measured by a C/25 charge step (delithiation). The cells then underwent several formation cycles for the SEI formation on the Li counter electrode in the following order: 2× C/10, 2× C/5, 2× C/2 with CC-CV charge and CC discharge. For the anode half cell, the CV phase was performed during discharge (lithiation) instead of charge. After the formation, the NCA half cells are characterized by a standard cycle consisting of a C/2 CC-CV charge and a C/5 discharge, followed by a pOCV with C/25, and a rate capability test with a C/10 CC-CV charge and varying discharge rates of C/10, C/5, and C/2 with two cycles per C-rate. The anode half cell is characterized by a C/2 CC-CV discharge and a C/5 charge, followed also by a pOCV with C/25 and a rate capability test with a CC-CV discharge of C/10 and varying charge rates of C/10, C/5, and C/2, also with two cycles per C-rate.

3. Results and discussion

The degradation of the 21700 cells is first characterized by the electrochemical measurements performed during the check-up tests. This includes the capacity fade of the cells, the DVA with the calculation of the underlying aging modes, the analysis of the EIS to separate the resistance increase of different processes as well as the analysis of Li plating. This is followed by post-mortem analysis of the aged cells by visual inspection, SEM/EDS, XRD and electrochemical characterization.

3.1. Capacity fade

Fig. 2 shows the SoH, which is the capacity measured in the check-up test relative to the capacity measured at BoL, plotted against the number of cycles for three cells cycled at each investigated temperature, i.e. 10 °C, 25 °C and 35 °C. At all temperatures, the SoH initially decreases linearly. However, at 10 °C and 25 °C, the cells exhibit a sudden decrease of SoH already before reaching 80 % SoH, which is commonly used as an end-of-life (EoL) criterion for EV applications. Such a sudden failure of the battery, characterized by a superlinear aging trajectory, is often

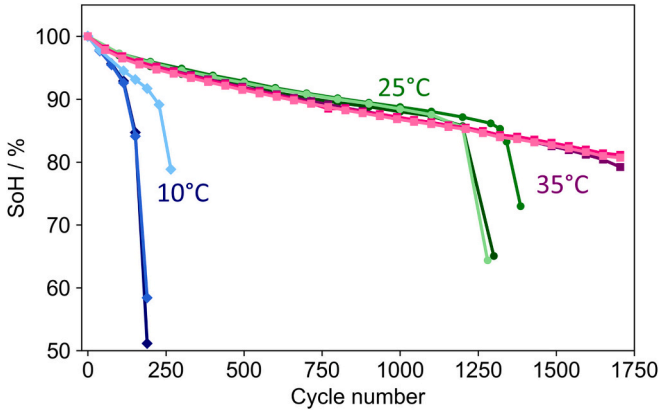

Fig. 2. SoH over cycle life for aging experiments performed with 3 cells for each aging temperature at 10 °C, 25 °C and 35 °C. The SoH is derived from the capacity measured in the check-up tests with 1C discharge at 25 °C.

referred to in the literature as "sudden death" or "knee point" [55]. The number of cycles before the sudden failure varies slightly between the cells cycled at the same temperature. At 35 °C, no sudden failure was observed for any of the cells. The linear decrease of SoH at the beginning of cycling is also temperature dependent with the highest decrease at 10 °C, resulting in a low total number of cycles of less than 250 cycles. In addition, the linear decrease is slightly higher at 35 °C than at 25 °C. Thus, the linear capacity fade is the lowest at 25 °C. However, the cells reach EoL first at 25 °C due to a sudden failure of the cells. Therefore, different aging mechanisms appear to be dominant at different temperatures which is in accordance with the results from Waldmann et al. [27]. They showed that at low temperatures Li plating is a dominant aging mechanism, whereas at higher temperatures cathode degradation and SEI growth becoming more pronounced. The different aging modes and mechanisms present in this study will be further discussed in the following by DVA and EIS data as well as post-mortem analysis.

3.2. Differential voltage analysis

The DVA is a powerful tool to analyze the degradation modes during aging without opening the cells. First, the peaks in the differential voltage (DV) curve are assigned to each electrode. Then, the change of the peak position is used to analyze the dominant degradation modes.

3.2.1. Correlation of half-cell to full-cell differential voltage curves

The DV curves are derived from the discharge of the pOCV measurement (C/25) of the check-up tests to analyze the degradation modes of the cells under the investigated cycling conditions. The peaks in the DV curve are inflection points of the OCV curve and thus represent single phase regimes between phase transitions [8]. They are assigned to the corresponding electrode using half-cell measurements from both electrodes. Fig. 3a shows the pOCV discharge curves of the 21700 cell and the GITT-OCV discharge curves of both electrodes while Fig. 3b depicts the corresponding DV curves. By shifting the half-cell potentials, the electrode level anode and cathode DV peaks can be correlated to the peaks of the 21700 cell. Since the anode is a blend electrode containing graphite and Si/SiO_x, the assignment of material specific losses is more complex. However, during discharge at low current rates, graphite is delithiated before silicon due to the large voltage hysteresis of silicon during (de-)lithiation [56]. Therefore, the contribution of both active materials can be separated by DVA of the discharge [8]. During (de) lithiation, graphite undergoes several phase changes [57–59]. Thus, the peaks of the anode in Fig. 3b can be correlated from left to right to graphite stage 2, stage 2L, stage 3L and stage 4L. The last two peaks can be assigned to the delithiation of Si which occurs above the potentials of the graphite phase transitions, starting above 230 mV vs. Li/Li^+ [13,56,60]. All peaks of the anode are clearly visible in the full-cell DV curve at BoL. In comparison, only two of the four peaks of the cathode active material NCA can be identified in the full-cell DV curve [43], which, as we will show later, can impede the quantitative assessment of cathode-related aging.

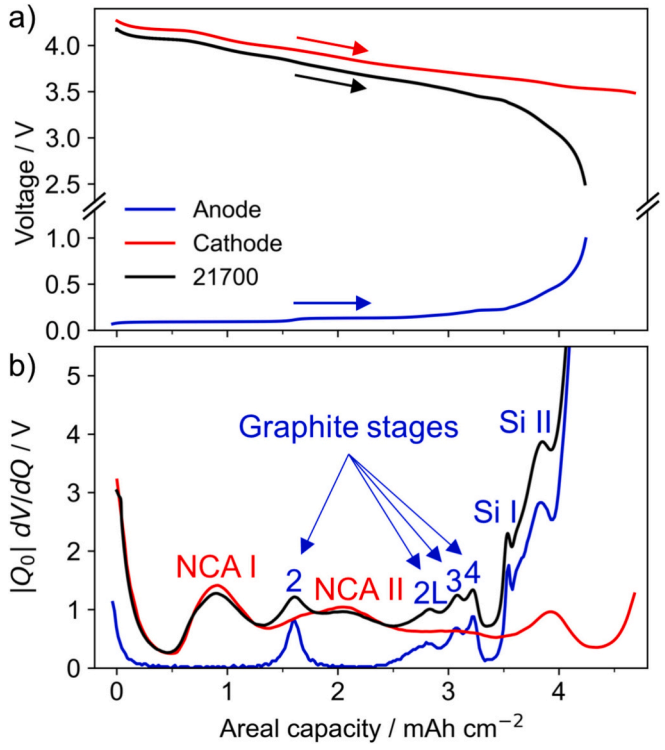

Fig. 3. (a) pOCV of 21700 cell correlated with GITT-OCV measurements of half cells and corresponding (b) DV curves. In (b), the peaks of the DV curves are assigned to the different active materials of the anode (graphite and silicon) and cathode (NCA) based on the half-cell DV curves.

3.2.2. Changes in the full cell differential voltage curve with aging

The aging modes can be derived from the changes in peak position and width with aging [6–9,16,61–63]. A shift between both electrodes indicates LLI. A decrease in the distance between two peaks of the same electrode can be attributed to LAM of that electrode. In the case of a blend electrode, the evaluation of LAM is more complex [8]. The active materials might degrade at different rates. Therefore, the LAM of the anode is evaluated separately for both active materials, e.g. LAM_{Si} and LAM_{Gr}. For the evaluation, features of interest (FOI) in the DV curve are selected and searched via a peak search algorithm in Python to calculate LAM and LLI from the changes of the DV curve over the course of aging (see Fig. 4). For the separation of the capacity of graphite and Si, the minimum between peak stage 4L and the first Si peak is used (AN2 in Fig. 4). The minimum at AN2 corresponds to the phase transition from stage 4 to stage 1L which occurs at 219 mV vs Li/Li^+. The delithiation of Si starts slightly above at 220 mV vs Li/Li^+ [8,56]. Therefore, the capacity above this minimum can be correlated mainly to silicon, and thus, the capacity of silicon Q_4 extends from AN2 to the end of discharge. A reduction of this capacity during aging is assigned to LAM_{Si}. To evaluate LAM_{Gr}, the change of the capacity Q_3 from AN2 to the peak of graphite stage 2 (AN1) is considered. The position of the cathode peak CA is analyzed to determine Q_2, from which LAM_{NCA} is defined. It was considered to include the second cathode peak in the DV curve analysis. However, this peak is relatively flat making it difficult to correctly assign the maximum peak position over aging. The evaluation of LLI is slightly more complex. First, the distance Q_1, the capacity until peak AN1, is evaluated. The decrease of this distance is due to LAM on the anode side as well as LLI. Since mostly graphite is delithiated in the voltage range of Q_1, LAM_{Gr} needs to be subtracted from Q_1 which results in following

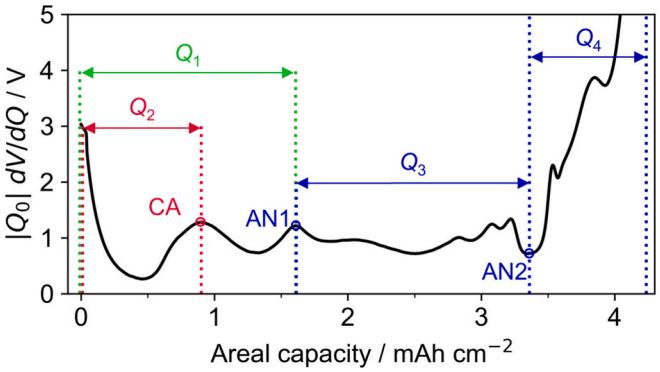

Fig. 4. DV curve of the discharge of the 21700 cell marked with the FOIs CA, AN1and AN2 as well as the capacities Q_1–Q_4 calculated by the distance of the FOIs.

equation for LLI:

$$LLI = \frac{Q_{1,BOL}(1 + LAM_{Gr}) - Q_1}{Q_{tot,BOL}} \quad (1)$$

Fig. 5a–c show the DV curves of the cells cycled at 10 °C, 25 °C and 35 °C that were opened later for post-mortem analysis. At all temperatures, the cathode peaks do not change significantly. In contrast, the anode peaks shift all to the left with increasing aging. Additionally, the first Si peak (Si I) becomes less pronounced with every check-up test. At 25 °C, the peak of graphite stage 2 (AN1) becomes broader and merges into CA. For this reason, the evaluation of AN1 is more elaborate. The change of the peak position of CA is minor, and therefore, the half-cell DV curve of the cathode (see Fig. 3b) is subtracted from the full-cell DV curve (see Fig. S1 in the Supplementary Information) to evaluate AN1 in this case. At 10 °C, AN1 becomes also broader, however, it can still be differentiated from the cathode peak without further analysis. The broadening of the peak is an indication for inhomogeneous delithiation of the anode [63]. In contrast, AN1 becomes sharper with increased cycle life at 35 °C. Note that due to a calibration of the battery cycler after the first two check-up tests at 25 °C, we observed a higher capacity in the C/25 cycle in the third check-up test (see Fig. 5b), although the cells continuously lose capacity in the reference cycle. Thus, only at low C-rates an increase of the capacity is observed, which is attributed to changes in the measurement set-up due to the calibration. To calculate the results of the DVA, the average BoL capacities of the cells aged at 10 °C and 35 °C are used as the BoL values at 25 °C.

3.2.3. Degradation modes based on the differential voltage analysis

The results for different LAM, LLI and the overall capacity loss are plotted in Fig. 5d–f. The last check-up tests after the sudden failure of the cells cycled at 10 °C and 25 °C are excluded in Fig. 5d–e because the sudden failure occurred after different cycle numbers leading to a large variation between different cells. At 25 °C in Fig. 5e, the evaluation of LAM and LLI starts at the third check-up test after 200 cycles due to the calibration of the battery cycler in between the measurements.

According to DVA, LAM_{Si} and LLI are the most severe degradation modes at all temperatures, while LLI is the limiting degradation mode. However, due to the higher cycle numbers at EoL for 25 °C and 35 °C, especially LAM_{Si} becomes more significant at these temperatures, although LLI is still limiting. In contrast, LAM_{Gr} and LAM_{NCA} increase only slightly with increasing cycle number, even at 35 °C. At 10 °C and 25 °C, the variation between the three tested cells is higher than at 35 °C. At higher temperatures, inhomogeneities due to temperature gradients inside the cell are less pronounced due to lower resistances and faster processes. Thus, the cells age more homogeneously at higher temperatures which could result in less variation between different cells.

In particular, for the cells aged at 10 °C, the capacity in the pOCV cycle is significantly higher than in the reference cycle with a 1C discharge, which is used to track the capacity loss (see Fig. 2). This suggests that the resistance increase plays a significant role for cells aged at 10 °C. To gain further insight, the resistance increase is analyzed in detail by EIS in the next section.

3.3. Electrochemical impedance spectroscopy

EIS was performed during check-up tests to investigate the influence of aging on the individual resistances of the cell, which can be separated by analyzing the impedance spectra with an ECM. To find a suitable ECM and to evaluate the contributions of both electrodes, DRTs of impedance spectra at different SoCs and temperatures are analyzed. Additionally, the change of the DRT during aging as well as a comparison with the results of the ECM are presented below.

3.3.1. Process identification by distribution of relaxation times

The SoC dependence of the EIS of the 21700 cell are shown in a Nyquist plot in Fig. 6a. The overall impedance is the highest at 0 % SOC and decreases in the mid-SoC range before increasing again slightly at high SoCs. The corresponding DRT is shown in Fig. 6d. Four processes have been identified (F1–F4) in the mid-frequency range of the full cell, all of which depend on the SoC. To correlate these processes to the corresponding electrode, the DRT of the full cell is compared with DRTs of each electrode (see Fig. 6b, c). The SoC-dependent impedance spectra

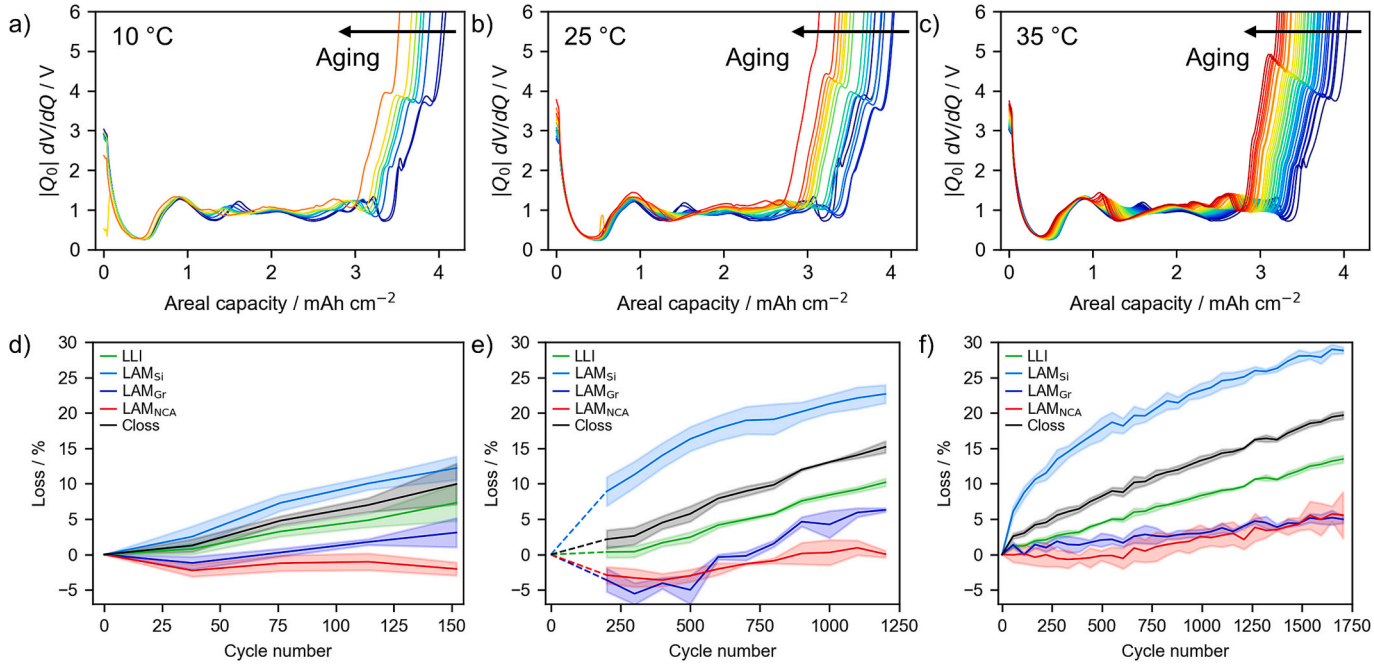

Fig. 5. DV curves over cycle life for cells aged at a) 10 °C, b) 25 °C and c) 35 °C. The corresponding averaged losses in % calculated by DVA due to LLI and LAM of graphite, silicon and NCA vs. cycle number for cells aged at d) 10 °C, e) 25 °C and f) 35 °C. The shaded areas show the standard deviation of three cells at each aging temperature. Due to a calibration of the battery cycler before the third check-up measurement at 25 °C, the values at the beginning of aging are taken from the other BoL tests.

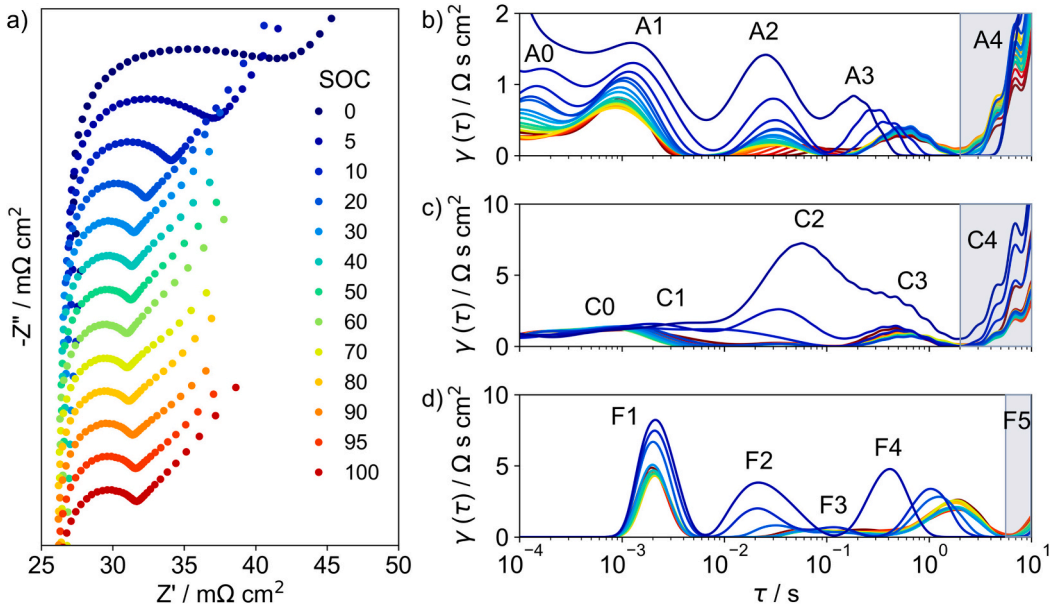

Fig. 6. a) Nyquist plot of EIS of the 21700 cell at BoL at varying SoCs, b) DRT of anode impedance measurement at varying SoCs (5 % SoC steps), c) DRT of cathode impedance measurement at varying SoCs (5 % SoC steps) and d) DRT of EIS measurements from a). Gray area in b–d) is showing the begin of the low frequency regime dominated by diffusion processes (A4, C4, F5).

of the electrodes, which are used for DRT, have been published by the authors in the parameter study of this cell [1], where the details of the experimental test procedure can be found. The impedance was measured in a three-electrode configuration with a Li reference ring, and thus, the DRT should only reflect the processes of the working electrode under investigation. Due to the high inductance present in the cylindrical cell caused by the cell windings, only processes measured in the three-electrode set-up above $\tau = 10^{-3}$ s are relevant for the comparison. Processes at lower time constants are included in the ohmic resistance R_Ω of the cylindrical cell [22].

For both electrodes, three peaks can be identified in the time domain above $\tau = 10^{-3}$ s (A1–A3 for anode, C1–C3 for cathode) and another one at a lower time constant (A0 for anode, C0 for cathode). The diffusion processes start between τ = 1–10 s (A4 for anode, C4 for cathode). However, the correct calculation of the diffusion processes by DRT is difficult, and thus, the results of the DRT in this time domain should be taken with caution. All processes in the mid-frequency range, A1–A3 as well as C1–C3, are SoC dependent with a significant increase of the peaks for SoCs below 15 % SoC and only negligible changes at higher SoCs. The intensities of the anode peaks A1, A2 and A3 gradually increase below 15 % SoC (see Fig. 6b). In addition, peak A3 shifts significantly to lower time constants while A1 and A2 only shift slightly. For the cathode, peaks C1–C3 increase significantly at 0 % SoC, especially C2, although this peak becomes negligibly small above 10 % SoC. For the cathode, no peak shift is visible. The first processes of each electrode, A1 and C1, can be attributed to the SEI and CEI resistances (R_{SEI}). The other peaks are assigned to the charge transfer resistances (R_{ct}) of both electrodes due to the frequency range but also SoC dependency [64,65]. Zhu et al. [66] assigned this first peak in DRT to the contact resistance between particles and current collector. However, the authors of this paper, in agreement with the work of Illig et al. [22], believe that this process occurs at a higher frequency and is only visible in the impedance measurements of the experimental cells (A0 and C0) because it is masked by induction in the cylindrical cell.

Table 1 shows the correlation of the peaks of the DRT of the individual electrodes to the full cell DRT based on their SoC dependence and the time constants of the processes. EIS measurements at different temperatures were also analyzed by DRT and support this correlation (see Supplementary Information Fig. S2), as they follow the same trend

Table 1
Correlation of the different processes visible in the DRT of the individual electrodes with the processes of the 21700 cell. The corresponding elements in the ECM are also listed.

Process description	DRT electrode	DRT 21700	ECM
Ohmic resistance	–	–	R_Ω
SEI/CEI resistance	A1 + C1	F1	R_{SEI}
Cathode charge transfer resistance	C2	F2	
Charge transfer resistance (dominated by cathode)	A2 + C3	F3	$\sim R_{ct,1}$
Anode charge transfer resistance	A3	F4	$\sim R_{ct,2}$
Diffusion resistance	A4 + C4	F5	W

in the half and full cells. The DRT of the individual electrodes have the same number of processes and similar time constants as the results from Wildfeuer et al. [21] for a 18650 cell with the same chemistry. However, we can identify four processes in the mid-frequency region in the DRT of the full cell at different SoCs and temperatures, while Wildfeuer et al. only identified three processes [21]. This difference could be due to variations in the active material, Si content and balancing of the cell.

3.3.2. *Changes in the distribution of relaxation times during aging*

Fig. 7a–c shows the DRTs of the impedance spectra measured at 50 % SoC at 25 °C in the check-up tests during aging at different temperatures. Interestingly, F1 is significantly larger at BoL than in the following check-up test after which F1 gradually increases again. This is observed at each temperature and could be due to a more stable SEI after some break-in cycles, which reduces the SEI resistance as shown in literature [36,67]. In addition, the time constant of F1 shifts during aging. Since this shift is temperature dependent, the underlying mechanisms responsible for this shift should also differ for different temperatures. Process F2 was observed at low SoCs in Fig. 6d. However, at 50 % SoC, F2 is not visible at BoL (see Fig. 7a–c). At 10 °C, no separate peak for F2 develops until EoL, whereas at higher temperatures, F2 becomes more pronounced in each check-up test. F3 increases similarly at all temperatures during aging, whereas F4 increases noticeably only at 10 °C. Both processes shift to higher time constants at all temperatures during aging. Process F5 increases also with aging, but remains at the same frequency.

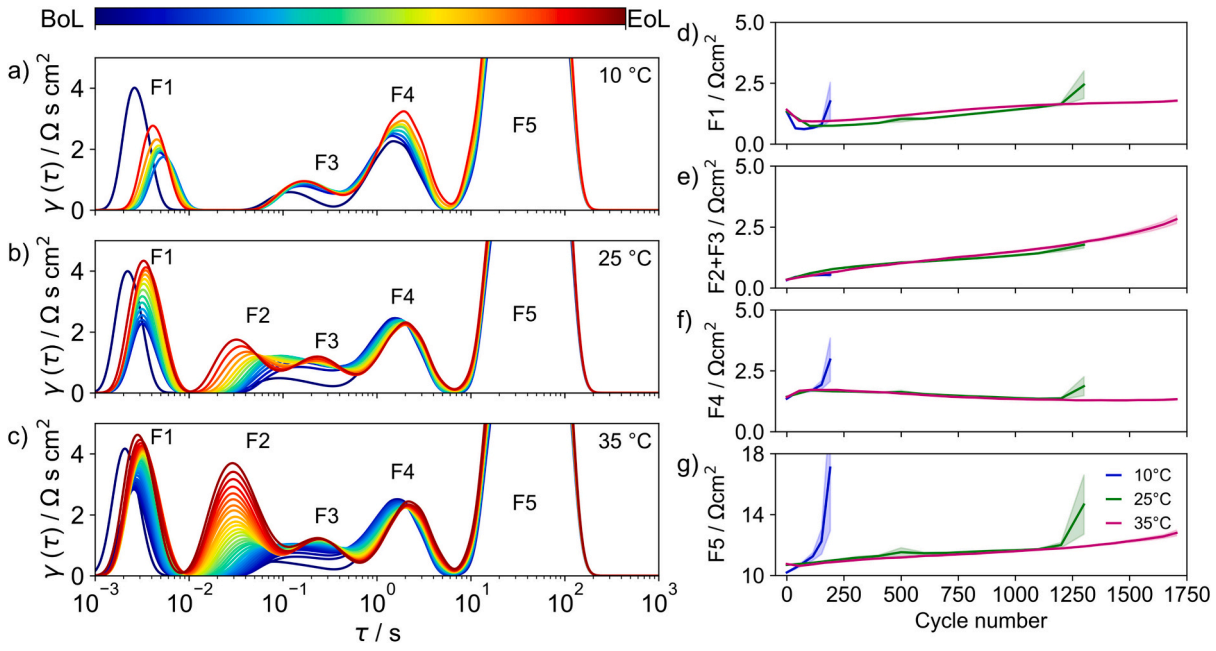

Fig. 7. DRT in the mid-frequency range of the impedance spectra measured at 50 % SoC in the check-up tests at 25 °C during aging at a) 10 °C, b) 25 °C and c) 35 °C from BoL (dark blue) to EoL (dark red). The peaks are labelled F1, F2, F3, F4 and F5 according to the assignment in Fig. 6 (see Fig. S3 in the Supplementary Information for zoomed-out version of the plot). The evolution of the averaged integrals of d) F1, e) F2 + F3, f) F4 and g) F5 vs. cycle number during aging at 10 °C (blue), 25 °C (green) and 35 °C (purple). The shaded areas show the standard deviation of three cells at each aging temperature. (For interpretation of the references to color in this figure legend, the reader is referred to the web version of this article.)

Since this process is significantly larger than the other processes, the increase of F5 during aging is shown in Fig. S3 in the Supplementary Information in a zoomed-out version of Fig. 7a–c.

To analyze the DRT quantitatively, we calculated the integral of $\gamma(\tau)$ for the processes shown in Fig. 7a–c. Since F2 and F3 are difficult to separate at the beginning of aging and even up to EoL at 10 °C, they are fitted together representing mainly the cathode R_{ct}. The quantitative evaluation in Fig. 7d–f shows that until the sudden failure of the cells, primarily the resistances of the processes F2 and F3 increase significantly. However, after sudden death, F1 and F4 increase considerably. The cells that are cycled at 35 °C do not show a sudden increase in resistance, as there is no sudden drop in capacity either. F2 and F3 seem to be independent of the aging temperature, whereas the increase of F1 varies for different aging temperatures. These results indicate that at 25 °C and 35 °C, the impedance increase is mainly attributed to SEI growth (F1) and the increase of the cathode charge transfer resistance

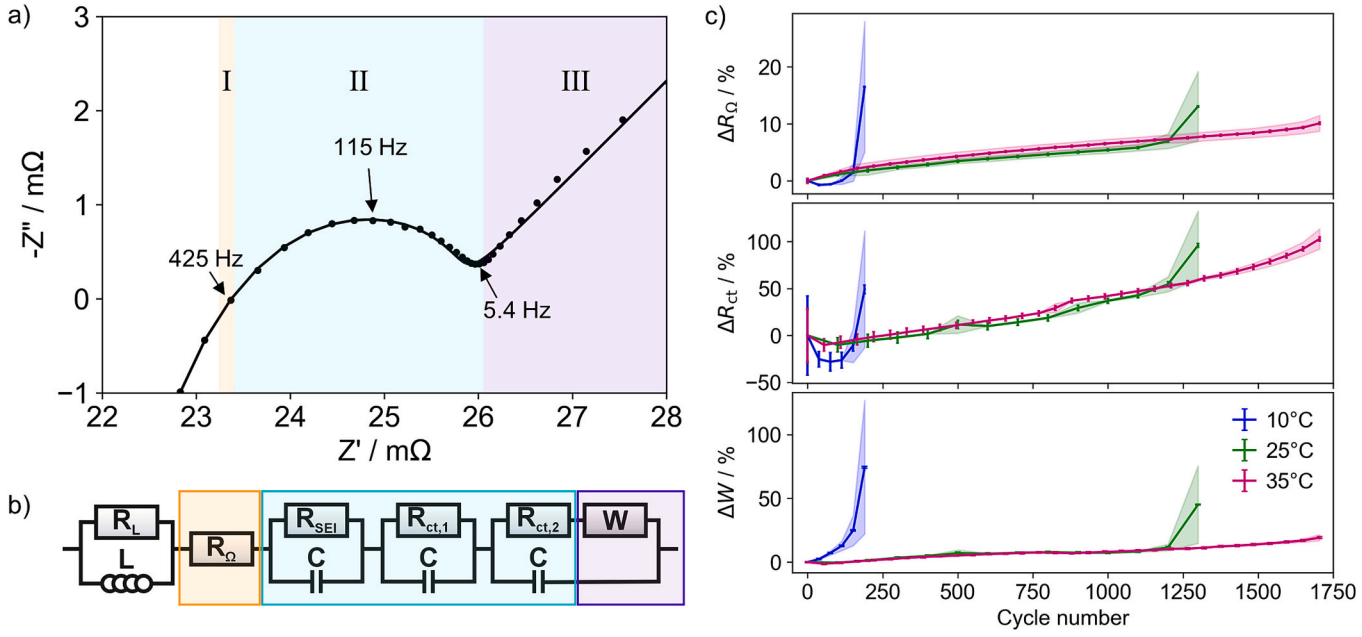

Fig. 8. a) Nyquist plot of EIS measured (dots) at 50 % SoC at BoL and the corresponding fit (solid line); b) ECM used for fitting the measured EIS; c) Change of R_{Ω}, R_{ct} (sum of R_{SEI}, $R_{ct,1}$ and $R_{ct,2}$) and W in % vs. cycle number for cells aged at 10 °C (blue), 25 °C (green) and 35 °C (purple). The error bars are the fit error and the shaded areas show the standard deviation of three cells tested at each aging temperature. (For interpretation of the references to color in this figure legend, the reader is referred to the web version of this article.)

R_{ct} (F2 and F3) in the mid-frequency range. However, at 10 °C, no significant increase of the cathode R_{ct} is observed due to the low cycle number. Instead, the anode R_{ct} (F4) increases significantly, which is not observed at higher temperatures. The diffusion resistance F5 shows a quasi-linear increase at the beginning with a sudden increase at the knee point, which leads to a significant increase of the overall impedance. Although the diffusion part of the DRT needs to be regarded with caution, we can see a very good agreement with the results of the ECM, which will be further discussed below.

3.3.3. Equivalent circuit modeling of impedance spectra

Although the DRT analysis provides valuable insight into the aging behavior of the cells, not all resistances can be extracted by DRT, e.g. the ohmic resistance. Therefore, the EIS are fitted with the ECM shown in Fig. 8b using the RelaxIS 3 software. Fig. 8a shows the Nyquist plot of an EIS measurement (dots) of the 21700 cell at 50 % SoC in the first check-up test before cycling. The spectra can be divided into high, mid and low frequency regions. The high-frequency region is dominated by inductive processes (L), mainly caused by wires and cell windings, and by the ohmic resistance R_{Ω}, the intersection of the spectra with the real axis [68,69]. R_{Ω} is the sum of all ohmic resistances of the cell and is influenced by the conductivity of the electrolyte and the specific cell design, e.g. the thickness and conductivity of the electrodes and current collectors as well as the number of tables [1,68,70]. In the mid-frequency range, three processes have been identified by DRT and are described in the ECM by a resistor and a capacitor in parallel. A capacitor is used here instead of a constant phase element (CPE) to avoid overfitting of the ECM, which could lead to high errors of individual ECM elements. Often, the first semicircle is assigned to the transport through the SEI layer, and the following processes are assigned to the double layer capacitance and the charge transfer resistance of the electrodes [16–18,68,69]. The diffusion process is described by a Warburg diffusion element added in the last R-C element of the ECM in series to the resistor [18]. The results of the fit over aging are shown in Fig. 8c as percentage changes of the resistances. R_{SEI}, $R_{ct,1}$ and $R_{ct,2}$ are summed to R_{ct} in Fig. 8c, but are shown separately in Fig. S4 in the Supplementary Information. In general, they should be comparable to the resistances analyzed by DRT, i.e. $F1 = R_{SEI}$, $F2 + F3 = R_{ct,1}$ and $F4 = R_{ct,2}$. However, it seems that the ECM introduces an inaccuracy. Nevertheless, when comparing the sum of all charge transfer resistances (F1–F4), the results from DRT and ECM for R_{ct} are in good agreement (see Fig. S5 in the Supplementary Information).

The resistances R_{Ω}, R_{ct} and W increase similarly during aging at 25 °C and 35 °C until the sudden failure of the cells at 25 °C, which in turn leads to a sudden increase of all resistances. Until sudden death, the increase of R_{Ω} and R_{ct} is slightly lower at 25 °C than at 35 °C. For cells aged at 25 °C and 35 °C, R_{ct} increases significantly more in percentage than R_{Ω} and W until EoL. In contrast, at 10 °C, W increases more than R_{Ω} and R_{ct}, which first decrease slightly before all resistances increase significantly with the sudden failure of the cells.

3.3.4. Interpretation of impedance results

In literature, the increase of the resistances has been attributed to CL, LLI and LAM, similar to the evaluation by DVA [16,17]. The increase of R_{Ω} is ascribed to CL which is mainly caused by electrolyte decomposition, but also by current collector corrosion and binder decomposition [16]. The increase of R_{SEI} can be attributed to LLI due to the Li consumption during SEI growth. For R_{ct}, there is debate in literature as to whether it should be assigned to LLI [16,17,71] or LLI and LAM [15,18], while the increase of the Warburg diffusion is consistently ascribed to LAM [15–18,71]. Some authors assign the increase of R_{ct} mainly to LLI because SEI and CEI growth as well as Li plating affect the surface properties of the active materials [16,17]. However, LAM can also lead to an increase of R_{ct}. LAM consists mainly of electrode particle cracking and loss of electrical contact. For the cathode, also crystal structural disordering and transition metal dissolution contribute to LAM, while for the anode, graphite exfoliation is attributed to LAM in literature [2]. These aging mechanisms affect not only the bulk of the particles but also the surface, therefore affecting R_{ct} as well as the diffusion resistance. Hence, it is difficult to separate LLI and LAM based on EIS measurements. Nevertheless, EIS and DRT analysis provide valuable information about the change in kinetics due to aging.

The quasi-linear impedance rise of the R_{Ω} and R_{SEI} (F1) at the beginning of aging is primarily caused by a continuous SEI growth and the resulting electrolyte consumption [18]. SEI growth is temperature-dependent, and thus, both resistances increase faster at higher temperatures than at lower temperatures. It has been reported that Li plating results in a reduction of the anode R_{ct} [72–74]. However, during relaxation, this reduction returns to the baseline value before the occurrence of Li plating [72,74]. Nevertheless, Li plating leads to an accelerated SEI growth, electrolyte consumption and porosity reduction, resulting in an increase of R_{Ω}, R_{SEI}, W, but also of the anode R_{ct} at the knee point [18,75]. In contrast, the rise of the cathode R_{ct} (F2 + F3) in the DRT is the only resistance that does not show a rapid increase of the impedance with the sudden failure of the cell. The quasi-linear impedance rise seems to depend mainly on the number of cycles. The influence of the temperature can be neglected here. In contrast, it has been reported that higher temperatures lead to increased particle cracking and structural decomposition on the cathode side due to transition metal dissolution and oxygen removal [18]. However, the cycling profile applied in this study may play a more significant role in the degradation of the cathode R_{ct} than the temperature influence due to the application of less extreme temperatures.

3.4. Indications for Li plating

The cells cycled at 10 °C and 25 °C show a sudden capacity decay accompanied by a sudden increase of impedance. This knee in the aging trajectory could have several different causes [55]. However, due to cycling at the maximum recommended charging rate of 0.5C of the cell, it is likely that the cause of the sudden failure of the cells is significant Li plating. Therefore, we analyzed the cycling data for possible signs of Li plating. When Li plating occurs during charging, a voltage plateau is visible in the following discharge voltage curve [76–79] or relaxation voltage [44,74,80–85]. The plateau is the result of a mixed potential of plated Li and lithiated graphite (Li_xC_6). During relaxation, plated Li intercalates into graphite until the reversible plated Li is depleted, resulting in a voltage plateau of a mixed potential until only the relaxation potential of Li_xC_6 is measured. This voltage plateau can be observed as an inflection point or even a local minimum in the differential voltage curve dU/dt, depending on the amount of reversibly plated Li. Since this method analyzes the relaxation voltage, it is also referred to as differential open circuit voltage (dOCV) analysis [82]. The time $t_{stripping}$ until the minimum in the dU/dt curve is an indication of the amount of plated Li [44,74,81–83]. However, $t_{stripping}$ is influenced by the rate of Li stripping, which is directly related to the rate of Li intercalation into graphite [83]. Li intercalation, in turn, depends on the exchange current density and the solid state diffusivity of Li ions in graphite, which are both temperature sensitive parameters. This needs to be considered for the evaluation of measurements at different temperatures.

For cells cycled at 25 °C, a minimum in the dOCV appeared only in the last cycling tests, which correlates with the sudden failure of the cells, whereas no minimum was found for cells cycled at 35 °C. In contrast, for cells cycled at 10 °C, a minimum in the dOCV curve is observed already in the first aging cycles (see Fig. 9a). The first cycle after each check-up test varies from the following cycles due to a C/25 discharge at 25 °C before cycling. Under these conditions, the IR drop is smaller, especially compared to cycling with 1C discharge at 10 °C. This results in a lower capacity in the first discharge of up to 0.3 Ah compared to the first charge at 10 °C. At 10 °C, this leads to a smaller amount of plated Li or even no measured reversible Li plating in the first cycle after

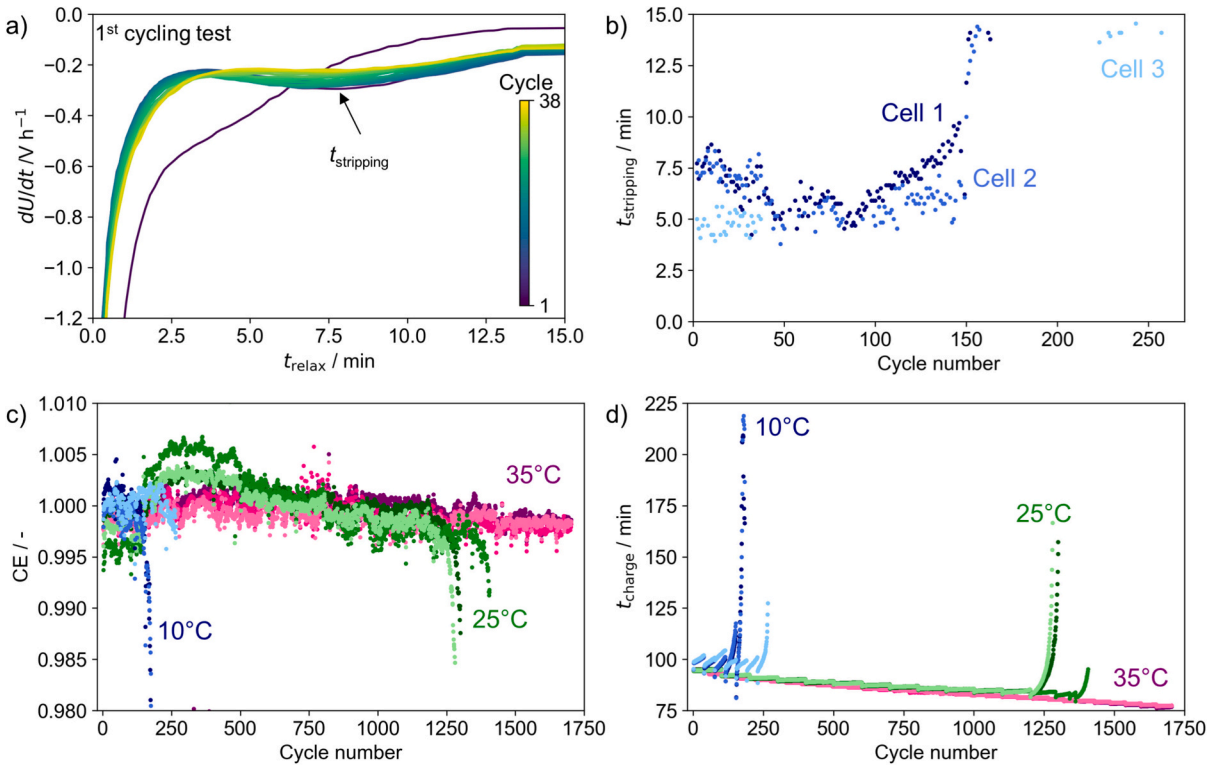

Fig. 9. Results of analysis of Li plating indications: a) differential voltage dU/dt vs. relaxation time t_{relax} for all cycles in the first cycling test of cell 1 at 10 °C; b) stripping time $t_{stripping}$ during relaxation for three cells cycled at 10 °C vs. cycle number as indicator for the amount of reversible plated Li; c) Coulombic efficiency (CE) of each cycle vs. cycle number for all cells cycled at 10 °C, 25 °C and 35 °C as indicator for irreversible plated Li (at the end of cycling at 10 °C and 25 °C); d) charging time t_{charge} of each cycle vs. cycle number for all cells cycled at 10 °C, 25 °C and 35 °C.

each check-up test. This emphasizes how important it is to have a map of the plating conditions as a function of SoC and temperature for fast charging of a cell to avoid Li plating. For two of the cells cycled at 10 °C, this minimum is observed throughout cycling until a sudden failure in less than 200 cycles (see Fig. 9b). Interestingly, for the third cell this minimum becomes less pronounced with cycling and finally disappears until it reappears in the last cycling test (see Fig. S6 in the Supplementary Information). Hence, for this cell, Li plating is less severe and the cell reaches more cycles. In the first cycles, the minimum appears after a shorter relaxation time than for the other two cells cycled at 10 °C. This means less Li is plated at the beginning of cycling, which could lead to an overall longer cycle life. However, this cell still has a significantly shorter cycle life compared to cells cycled at higher temperatures. Although no minima were observed, it is likely that a small amount of Li was still plated in each cycle. The amount of plated Li, indicated by $t_{stripping}$, also decreases for the two other cells that were cycled at 10 °C after the first cycles and increases again at the end of cycling. For all three cells cycled at 10 °C, no minima are observed in the last few cycles. This is likely due to massive Li plating, and thus, the 15 min pause is not sufficient for re-intercalation of plated Li. Our results support the findings from Mei et al. [85] that Li plating can develop in several stages. In their publication [85], they showed that initially no minima are observed in the relaxation period, but Li nucleation takes place. With increasing number of cycles, they observed a minimum during relaxation, attributed to a Li growth phase, until finally they did not observe a minimum anymore due to massive Li plating, where the stripping occurs until the subsequent delithiation of the graphite anode.

Massive Li plating could also be associated with a high percentage of irreversible Li plating, which can be estimated by a significant reduction of the coulombic efficiency (CE) during cycling [82]. Fig. 9c shows the change of the CE over cycle life. The baseline for the CE is between 99.5 % and 100.5 % during cycling, but as soon as the CE drops below 99.5 %, the CE decreases exponentially with every cycle, showing the on-set of irreversible Li plating, which leads to a sudden failure of the cell. This was observed for all cells measured at 25 °C and the two cells cycled at 10 °C, which drop below 60 % SoH. The third cell cycled at 10 °C was opened for post-mortem analysis at the on-set of irreversible Li. For cells cycled at 35 °C, no drop of the CE was observed. The decrease in CE correlates with an increase of the CV period during charging, which was observed for cells cycled at 10 °C and 25 °C (see Fig. 9d).

At 10 °C, Li plating conditions exist already at the beginning of cycling due to an increased resistance at low temperatures, which reduces the local potential on the anode side below 0 V vs. Li/Li$^+$. After the first few cycles, the amount of plated Li decreases, which could be a result of a shift of the half-cell potentials due to a significant LLI by irreversible plated Li and the associated SEI growth. In addition, the charge capacity is reduced after each check-up test. With continuous Li plating, especially the diffusion resistance increases as pores become clogged (see Fig. 7g and Fig. 8c), which again leads to an increase of Li plating by lowering the anode potential below 0 V vs. Li/Li$^+$. In contrast, at 25 °C, Li plating conditions suddenly appear after many cycles. Before the sudden failure of the cells, the resistances are similar to those of the cells aged at 35 °C (see Fig. 7 and Fig. 8). Thus, the resistance increase alone cannot be the reason for Li plating. Instead, the faster kinetics at 35 °C result in a more homogeneous charging process. Consequently, the risk of local Li plating is reduced, leading to a longer cycle life compared to 25 °C, despite a similar increase of resistances and losses due to LLI and LAM.

3.5. Post-mortem analysis

At each temperature, one cell is opened in the glove box under argon atmosphere after reaching 80 % SoH to compare the aging modes derived by electrochemical methods with the underlying degradation mechanisms. At 10 °C and 25 °C, the cells experienced a sudden failure, resulting in a sharp decline in capacity. Therefore, the cell with a

capacity closest to 80 % SoH was selected for post-mortem analysis. Prior to opening the cells, the SoH of those aged at 10 °C and 25 °C were 78.9 % and 73.0 %, respectively. Due to the consistent linear degradation at 35 °C, all the cells aged similarly throughout the testing period, reaching 80 % after the same number of cycles.

First, a visual inspection of the cells is performed to analyze any visible degradation. Then, SEM/EDS and XRD results are presented to provide further insight into the aging mechanisms. Finally, the electrochemical tests of the harvested electrodes give additional information on the electrochemical degradation of the active material.

3.5.1. *Visual inspection*

After opening of the aged cells, the electrodes were visually inspected to examine possible aging mechanisms such as Li plating. Fig. 10 shows images of both electrodes for different aging temperatures. At all temperatures, the anode looks more degraded than the cathode. The cathodes show a blue discoloration in the middle part of the sheet, especially at 25 °C and 35 °C. This is further analyzed by XRD and discussed in a later subchapter. The cathode coatings are still mechanically intact, however, at 10 °C, the core part of the cathode sheet is significantly deformed, which also leads to cracks in the coating (see Fig. S7 in the Supplementary Information). At each aging temperature, the anode sheet is deformed at the core part of the jellyroll and also, the coating is more brittle. During disassembly, the coating came off at the edges of the anode sheet, but also in the core part of the sheet (see Fig. 10b and c). At 25 °C and 35 °C, the coating also delaminated near the cathode current collector tab (see Fig. 10d). It is known that deformation occurs near the cathode tab since it is thicker than the cathode sheet [86]. Coating stability is affected by cycling due to the expansion of graphite of about 10 % [59] and Si/SiO_x of about 200 % [87] as well as the resulting mechanical stress when expansion is limited by space inside the cell [34]. Hence, more cycles result in a more mechanically unstable electrode. Thus, less coating came off for the cell cycled at 10 °C compared to the other temperatures. The Samsung INR21700-50E does not contain a center-pin, also called mandrel, to stabilize the electrode sheets in the center of the cell, which results in a more severe deformation in the core part of the electrode sheet [34].

In addition to the mechanical instability, a gray deposit, most likely irreversible plated Li, was observed covering some part of the anode sheet. In particular, on the core part of the anode sheet of the cell aged at 10 °C, a large amount of gray deposit is found at the edge of the electrode sheets as well as in the center of the sheet (see Fig. 10c). The deposition forms a pattern showing that the amount of deposition depends on the radial position within the 21700 cell. At 25 °C and 35 °C, only a subtle pattern without any gray deposits can be observed on the core part of the anode sheet (see Fig. 10c). However, at 25 °C, the coloration of the pattern is similar to the color next to the gray deposits close to the cathode current collector (see Fig. 10d) and has a metallic shimmer. This coloration could be due to changes in the surface layer or due to inhomogeneous lithiation of graphite. Graphite turns from gray to bluish, then red and finally golden with increasing lithiation degree [88]. Thus, the bluish coloration could be due to an inhomogeneous lithiation of graphite. However, it is also likely that reversible lithium plating occurred at this location, leading to a change of the SEI and would explain the metallic shimmer. This metallic shimmer is also apparent on the anode sheet at 10 °C. Gray deposits are also found on the anode sheet near the current collector tab of the cathode, although the amount is significantly less at 35 °C (see Fig. 10d). This is in fact the only location where Li deposits could be clearly identified at 25 °C and 35 °C. Li plating close to the cathode tab under mild cycling conditions has also been reported by Smith et al. [89]. Qiu et al. [90] showed that deformation could accelerate the initiation of Li plating, which would explain the Li deposits close to the cathode tab as well as the lithium deposition in the core part of the cell. According to Qiu et al. [90] Li plating is more likely to occur at the edges of the sheets and around the exterior of the jelly roll due to temperature gradients and locally lower temperatures. Although we observed Li plating at the edges of the anode sheet at 10 °C, we did not observe any significant plating at the outer end of the sheets, but mainly in the core part. It is likely that the deformation of the electrode sheet and an increased local higher resistance led to Li plating in this area. The degree of deformation most likely varies slightly between cells and would explain the variation of sudden failure between cells cycled under the same conditions.

3.5.2. *SEM/EDS*

SEM/EDS top view images of the electrodes were prepared to examine changes in their microstructure. SEM top view images of BoL and aged anodes are shown in Fig. 11 at 3000× magnification. A change in the surface layer is clearly visible for the aged anodes, especially for the anode aged at 10 °C. At BoL, the contours and the surface of the anode particles are clearly visible. Although the individual particles can still be distinguished for the anodes aged at 25 °C and 35 °C, it appears that the surface layer is thicker and therefore, the surface structure is less distinct than at BoL. At 10 °C (see Fig. 11b), however, no contours or surfaces of the graphite particles can be identified. Instead, a thick porous surface layer with smaller and larger cracks covers the particles.

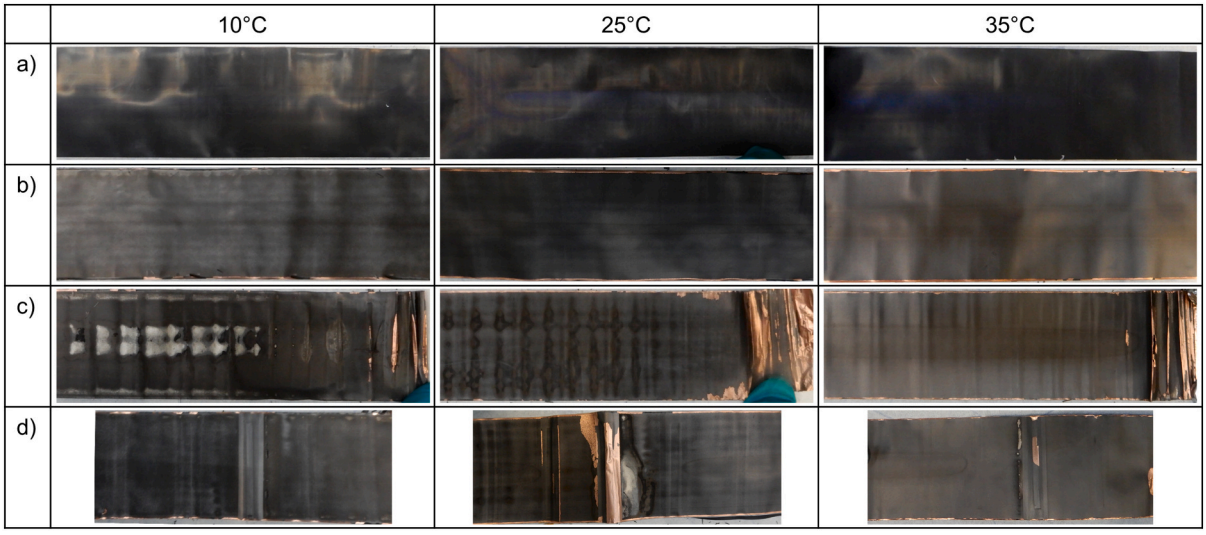

Fig. 10. Visual inspection of electrode sheets extracted from aged 21700 cells at different temperatures (10 °C, 25 °C, 35 °C): a) cathode sheet, b) outer part of anode sheet, c) core part of anode sheet, d) anode close to cathode current collector tab.

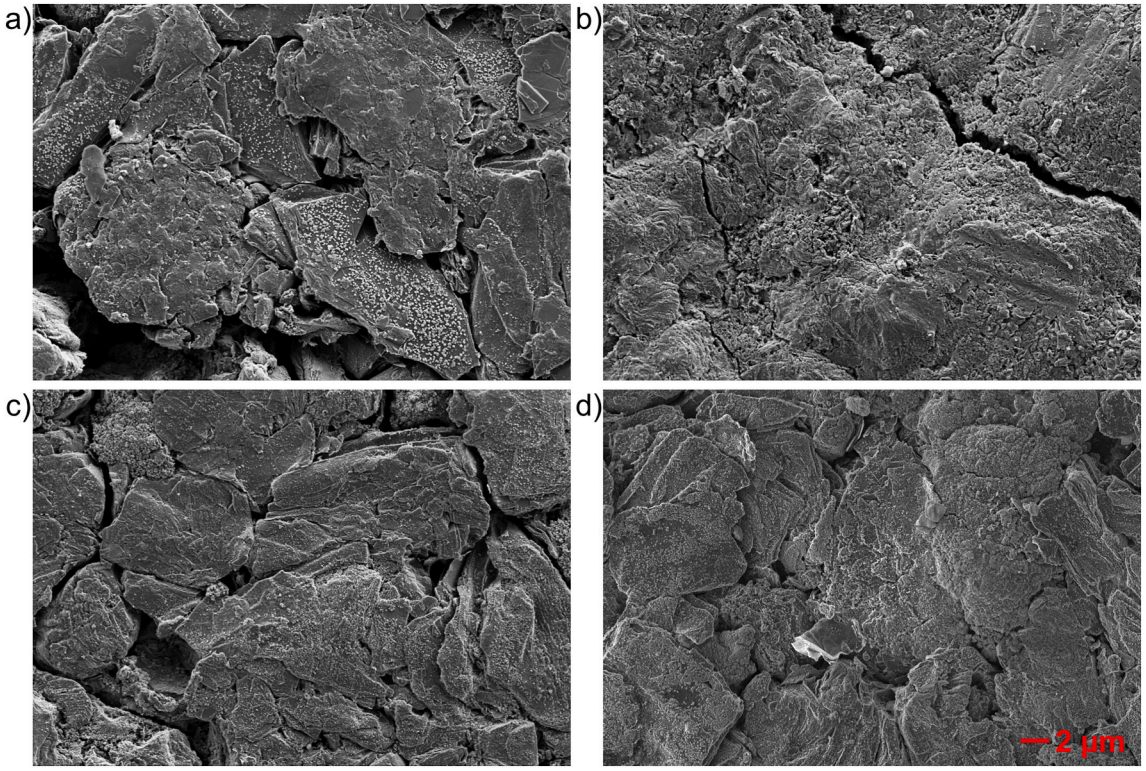

Fig. 11. SEM images with a magnification of 3000× of the anode surface from a) a BoL cell and aged cells cycled at b) 10 °C, c) 25 °C and d) 35 °C.

In addition to the SEM images obtained with the secondary electron detector, images of the anode surface were taken with a backscattered electron (BSE) detector (see Supplementary Information Fig. S8). Since the number of backscattered electrons reaching the detector is proportional to the atomic number of the material, graphite and silicon can be distinguished by different shades of gray. Although EDS is not suitable for quantitative analysis, these BSE images together with EDS measurements indicate that at 10 °C the surface layer on graphite particles is thicker than on silicon particles (see Figs. S8 and S9 in the Supplementary Information). The surface layer on the graphite particles is too thick to see the contours of the particles, however, the silicon particles are still visible in the BSE images. In comparison, for the sample from the cell aged at 25 °C, the particle contours of both active materials of the blend electrodes are still visible, although a surface layer is clearly visible.

Thick surface layers on graphite electrodes cycled at low temperatures could be the result of continuous Li plating, which leads to increased SEI formation [78,91]. The samples examined here did not show any gray deposits on the surface, yet the surface layer is very thick at 10 °C. At other positions of the electrode, a gray deposit was visible, indicating Li plating (see Fig. 10c, d). Therefore, it can be assumed that the thick surface layer present at 10 °C in Fig. 11b is also a result of Li plating. Here, the SEM and EDS results indicate that Li plating may be less severe on silicon particles compared to graphite particles in blend electrodes. Richter et al. [44] showed in an operando neutron diffraction study that at low temperatures Li first intercalates into graphite due to kinetic limitations and redistributes to silicon during rest periods. This may lead to less Li plating on the silicon particles, and therefore, to a thinner surface layer. This is consistent with a current simulation study of Bovoleth et al. [92], which showed that for typical material parameters plating preferentially occurs on graphite in graphite-silicon composite electrodes.

The SEM and EDS images of the cathode surface do not show any significant changes due to aging (see Fig. S10 in the Supplementary Information). A typical aging phenomenon are cracks of the secondary particles, which were already visible in the BoL images.

3.5.3. XRD

XRD is used to investigate any possible changes in the bulk phase of the active material that could lead to capacity loss. Fig. 12 shows the diffraction patterns of the examined samples. Two samples were measured at 35 °C, one with a blue discoloration. The diffractograms are investigated with Rietveld refinement to derive information about the lattice parameters and the microstructure. The results are listed in Table 2.

For the refinement of the cathode, the space group R-3m was used. No other phases can be observed for the aged samples. However, the *a*-lattice parameter decreases while the *c*-lattice parameter increases compared to BoL (see Table 2), suggesting a lower degree of lithiation for all EoL samples [36,93,94]. The cells were discharged with a low C-rate of C/25 before opening, hence, this is an indication for LLI.

Most changes are observed for the cathode aged at 25 °C. Only minor changes are observed between the blue and black location of the electrode at 35 °C. This indicates that the blue discoloration is a surface effect and not the result of a change in the bulk crystal structure of the active material. This surface effect could be further analyzed by surface sensitive methods like X-ray photoelectron spectroscopy (XPS) or Fourier transform infrared spectroscopy (FTIR), however, this is out of scope for this work. A significant reduction of the crystallite size of NCA occurs only at 25 °C, indicating a structural degradation of the active material. Interestingly, the crystallite size slightly increases for the electrodes aged at 10 °C and 35 °C, which could be due to slight local variations of the active material along the electrode.

In the diffractogram of the anode (see Fig. 12b), the intensity of (002)-reflection of graphite decreases significantly for the samples from the cells aged at 25 °C and 35 °C. The crystallite size of graphite increases slightly for the cell aged at 10 °C to 38.8 nm, but decreases for the cells aged at 25 °C and 35 °C to 33.1 nm and 32.5 nm, respectively. This indicates that the structure of graphite is slightly damaged after long-term cycling at 25 °C and 35 °C.

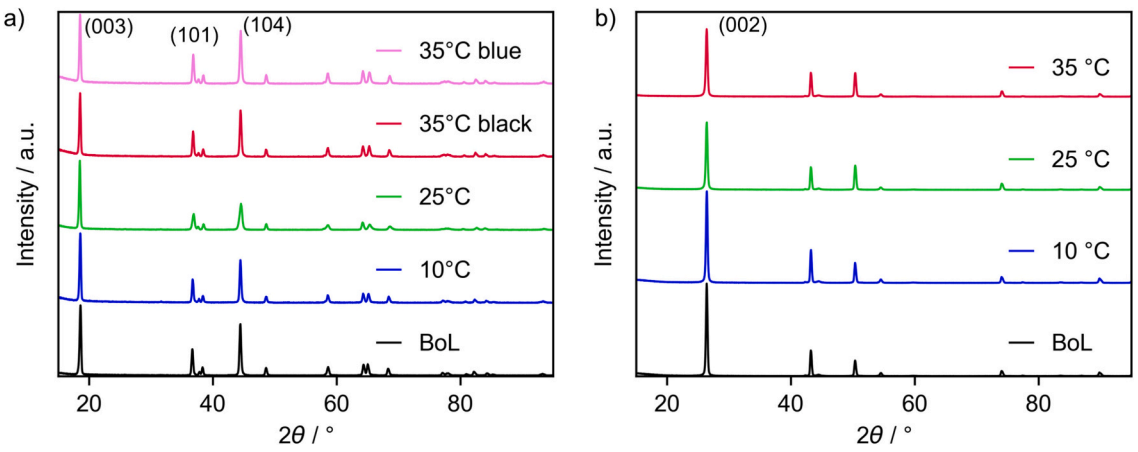

Fig. 12. XRD pattern of cathodes (a) and (b) anodes harvested from the 21700 cell at BoL and after cyclic aging at three different temperatures. Two locations of the cathodes were measured at 35 °C, one with a bluish discoloration.

Table 2
Parameters obtained by Rietveld refinement of XRD measurements of the cathode and the anode. For refinement of the cathode, the space group R-3m and a preferred orientation of the (0 0 3)-plane was used. For the anode, the space group P63/mmc and a preferred orientation of the (0 0 2)-plane was used.

	Unit	Cathode					Anode			
		BoL	10 °C	25 °C	35 °C black	35 °C blue	BoL	10 °C	25 °C	35 °C
a	Å	2.86170 (13)	2.85800 (13)	2.84740 (19)	2.85357 (18)	2.85231 (18)	2.4603 (7)	2.4608 (7)	2.4598 (7)	2.4600 (7)
c	Å	14.2276 (14)	14.2544 (14)	14.301 (2)	14.281 (2)	14.286 (2)	6.7189 (9)	6.7212 (9)	6.7213 (8)	6.7228 (7)
Crystallite size	nm	30.71 (14)	32.53 (16)	26.55 (16)	31.8 (2)	31.1 (2)	36.9 (10)	38.8 (14)	33.1 (10)	32.5 (9)
$L_{vol\text{-}IB}$	nm	28.85 (14)	30.56 (15)	24.94 (15)	29.9 (2)	29.22 (19)	34.7 (9)	36.5 (13)	31.0 (9)	30.5 (8)

3.5.4. Electrochemical tests

Measurements in a three-electrode set-up were performed to investigate LLI and LAM of each electrode separately by analyzing the capacity compared to BoL electrodes. LLI can be estimated by evaluating the residual capacity, which is the capacity that can be extracted by discharging the harvested electrodes in a half-cell configuration at a low current, i.e. lithiation for the cathode and delithiation for the anode [3,29,31,32,36]. Since the 21700 cells were fully discharged prior to disassembly, the differences in the residual capacity compared to BoL provide an estimate of the inaccessible Li in the aged cells. Fig. 13 shows that the residual capacity of the anode does not change between BoL and the electrodes harvested from the aged cells. Therefore, no Li was trapped in the anode due to a shift of the half-cell potentials during cycling. In contrast, the residual capacity of the cathode increases significantly with aging, which can be correlated to LLI, either by side reactions or by loss of lithiated active material. At BoL, the residual capacity is 7.1 % of the total cathode capacity. This corresponds to the LLI during the formation cycles of the 21700 cell. To calculate the LLI due to aging, the LLI lost during formation is subtracted from the total LLI measured in the cathode half cells. At 10 °C and 35 °C, the LLI determined from the residual capacity is 2.4 % lower than the values obtained from the DVA of the 21700 cells, whereas at 25 °C it is 2.8 % higher (see also Table 3). This could be due to inhomogeneities along the electrode sheet. The error bars for the residual capacities in Fig. 13 (obtained by taking three electrodes from different position within the electrode sheet) suggest that the inhomogeneity is the highest for the cells aged at 10 °C, whereas at 35 °C, the cells aged very homogeneously. Inhomogeneous aging is known to be a problem in cylindrical cells due to high temperature and current gradients inside the cells [29].

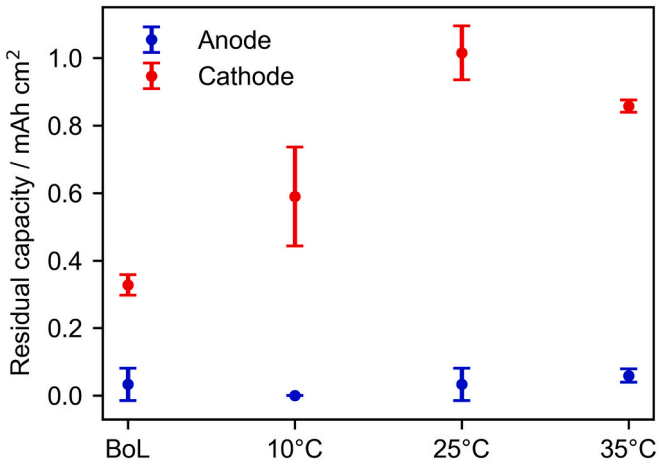

Fig. 13. Residual capacity measured for at least three cells each at BoL and electrodes aged at 10 °C, 25 °C and 35 °C.

To separate the contribution of graphite and Si to the anode capacity loss, DVA of the pOCVs of the half cells is conducted (see Fig. 14a). The minima in the DV curve before and after the silicon peaks (see Fig. 3b) are used to separate the capacity of graphite and Si. In the DVA of the pOCV in Fig. 14a, the peaks of Si I and Si II are difficult to separate compared to the DVA of the GITT-OCV curve in Fig. 3b. However, the minimum after the second Si peak is more pronounced in Fig. 14a. Fig. 14a shows that the proportion of silicon decreases significantly more than that of graphite for all EoL cells. Interestingly, the graphite peaks become more pronounced for aged anodes. This indicates a more homogeneous delithiation of graphite at EoL compared to BoL - at least for small areas of the electrode. This is in contrast to the peak broadening of AN1 (graphite stage 2) in the DVA of the 21700 cells during aging at 10 °C and 25 °C in Fig. 5, suggesting an increased inhomogeneity of the delithiation for aged cells. Table 3 lists the LAM of the anode (LAM_{Anode}), LAM_{Gr}, LAM_{Si} and LAM_{NCA} of the harvested electrodes and of the EoL 21700 cells in the last check-up before opening the cells. The total LAM on the anode side, LAM_{Anode}, at the cell level is calculated from LAM_{Gr} and LAM_{Si} considering a capacity share of 12.7 % of Si at BoL [1]. At 10 °C, LAM_{Anode} at the electrode and cell level show

Table 3
Measured LAM and LLI of the harvested electrodes (mean value of at least three half cells) and DVA estimation of LAM and LLI of the 21700 cells at EoL after aging at 10 °C, 25 °C and 35 °C.

in %	LAM_{Anode}		LAM_{Gr}		LAM_{Si}		LAM_{NCA}		LLI	
	Electrode	21700	Electrode	21700	Electrode	21700	Electrode	21700	Electrode	21700
10 °C	4.8	4.7	2.7	3.3	19.4	14.8	4.8	4.3	7.1	9.5
25 °C	12.2	10.0	9.3	8.0	31.6	24.3	8.5	1.3	15.0	12.2
35 °C	10.1	7.8	7.4	4.7	28.7	28.8	11.9	2.3	11.6	14.0

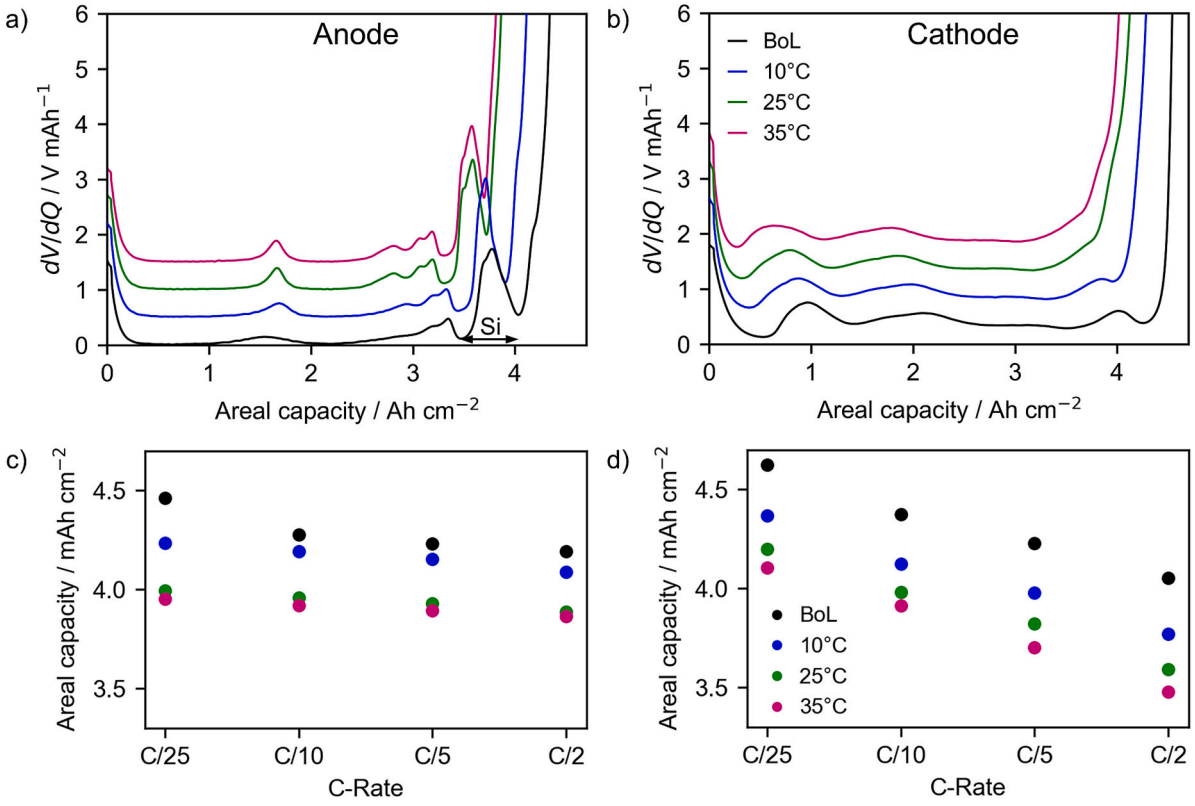

Fig. 14. DVA of pOCV during discharge (a, b) and rate capability (c, d) of GrSi anodes (a, c) and NCA cathodes (b, d) harvested from a BoL 21700 cell and cells after cyclic aging at 10 °C, 25 °C and 35 °C. DVA of the anode is used to separate the contributions of graphite and silicon to the overall LAM of the anode. In (a), the capacity contribution of silicon in the blend electrode is indicated.

very good agreement of 4.8 % and 4.7 %, respectively, although the electrode sheet was significantly deformed in the core part of the electrode leading to local delamination of the coating (see Fig. 10c). In contrast, at 25 °C and 35 °C, LAM_{Anode} is around 2 % higher at the electrode level than at the cell level. LAM_{Si} is significantly higher at the electrode level than estimated by the DVA of the full cell for the cells aged at 10 °C and 25 °C. However, at 35 °C, LAM_{Si} agrees well between both analyses. In comparison, LAM_{Gr} at cell and electrode level is similar at 10 °C and 25 °C, whereas at 35 °C, it is underestimated by 2.7 % at cell level. The discrepancy between the values measured at the cell level and the electrode level could be due to the overhang of the anode, inhomogeneities along the electrode sheet [47], local delamination of the coating, but also a limiting cathode capacity. However, the results show that the LAM of Si is more severe than that of graphite, both at the electrode and at the 21700 cell level. At the electrode level, the proportion of Si decreases over aging from 12.7 % to 9.1 %. This emphasizes that a separate consideration of graphite and silicon is necessary to evaluate the LAM of the negative electrode.

For the cathode, LAM_{NCA} at the electrode level is higher than estimated from the DVA of the 21700 cell at EoL for all aging temperatures (see Table 3). In particular, at 25 °C and 35 °C, LAM_{NCA} at the electrode level is 7.2 % and 9.6 % higher than at the cell level. Fig. 14b shows that the shape of the cathode half-cell DV curve changes significantly with aging. The peak on the left (NCA I) becomes broader and begins to split into two separate peaks for the aged electrodes. The distance between the peak on the right and the end of the DV curve decreases with increasing aging temperature, so that no peak maxima are visible anymore for the cathodes aged at 25 °C and 35 °C. This loss at the end of discharge is masked by LLI in the 21700 cell. Therefore, LAM_{NCA} is significantly underestimated by the full cell DVA. However, since it is not visible in the full cell DVA, it may not have a significant effect on the full cell capacity loss for the conditions studied here.

The peak shapes in the DV curve of the aged cathodes indicate that the lithiation becomes more inhomogeneous and/or a change of the crystal structure. However, no significant change of the bulk crystal structure was measured by XRD. In addition, a rate capability tests of the half cells were performed (see Fig. 14c, d). Although the loss of the capacity at C/25 is relatively high for the aged electrodes, it seems to have no effect on the rate capability of the electrodes. The rate capability up to C/2 is superior for the anode than for the cathode. Therefore, no significant degradation of the electrode microstructure can be observed that would lead to significantly lower electronic conductivity of the porous electrode network or ionic conductivity in the electrolyte-filled pores. This is in contrast to the increased resistances observed by EIS

of the 21700 cell. However, the resistance increase of the 21700 cell could also be due to local electrode degradation, electrolyte degradation, and separator blockage [4,48].

3.6. Degradation compared to literature

In the following, the overall results of this study are compared with studies from literature, focusing on cells with similar chemistry, particularly those using NCA as cathode active material and a blended anode of graphite and SiO_x. The results of this study demonstrate that temperature significantly affects the degradation of high energy NCA/graphite-SiO_x cells, even within a relatively narrow temperature range of 10 °C to 35 °C. In particular, lower temperatures resulted in an early onset of Li plating and inhomogeneous degradation, which ultimately resulted in a sudden failure of the cells. These findings are consistent with the work of Aufschläger et al. [47], who observed similar degradation behavior in cells of the same type cycled at 5 °C with a high charge rate of 1C between 50 % and 100 % SoC, as well as cells cycled at 0.5C and 100 % DoD at 25 °C. They used computer tomography (CT) to show that the non-linear capacity fade began prior to the deformation of the jelly roll [47].

Furthermore, cycling at a higher temperature of 35 °C resulted in a longer cycle life without a sudden failure compared to 25 °C, most likely due to a more homogeneous degradation as indicated by DVA. In comparison, Liu et al. [36] showed that even higher temperatures of 45 °C and 65 °C lead to a faster degradation of 10 Ah NCA/graphite-SiO_x pouch cells and ultimately to a sudden capacity fade. According to their post-mortem analysis, the faster degradation at high temperatures is due to an increased decomposition of the electrolyte as well as blockage of separator pores caused by decomposition products [36]. Although the decomposition of the electrolyte is temperature-dependent, it seems that the electrolyte of the cells investigated in our study remains relatively stable at 35 °C, and thus, the slightly higher electrolyte decomposition rate at 35 °C could be counterbalanced by the more homogeneous degradation of the cells. Mikheenkova et al. [48] also studied NCA/graphite-SiO_x cells at 45 °C, attributing the increased degradation rate primarily to the accelerated degradation of the NCA cathode, which is consistent with other studies that report higher degradation at elevated temperatures [17,18].

The addition of silicon to graphite in the anode results in a higher volume change during cycling, which increases mechanical stress [41,47]. This could lead to a more inhomogeneous degradation, particularly in cylindrical cells where space is limited. Therefore, incorporating silicon into the anode not only accelerates capacity fade due to silicon degradation and increased Li loss from increased SEI formation, but could also contributes to a more inhomogeneous degradation due to the high mechanical stress.

The cells in this study were cycled between 0 % and 80 % SoC, which resulted in extensive usage of silicon in each cycle. As reported in literature, cycling graphite-SiO_x cells at low SoC leads to a faster degradation due to the high utilization of silicon, which leads to rapid LAM as confirmed by DVA herein [34,47,48]. Although avoiding cycling to SoCs below 20 % in cells with graphite-SiO_x blend anode could reduce degradation, it would also reduce the usable capacity of the battery significantly. However, optimizing the charging protocol in the BMS based on temperature could improve the cycle life by preventing Li plating and taking advantage of the improved kinetics at elevated temperatures [70,95].

4. Conclusions

This study compares non-invasive electrochemical methods, namely, dOCV, DVA and EIS combined with DRT analysis with post-mortem analysis to identify the degradation modes and mechanisms of a commercial high-energy cylindrical 21700 cell at various temperatures. By combining dOCV, DVA and EIS, the main degradation modes and mechanisms were successfully determined without the need to open the cells. However, post-mortem analysis revealed that the severity of certain degradation modes, in particular the LAM of the cathode, was masked in the full cell by the dominating LLI.

From DVA, the dominant degradation modes were successfully identified to be LAM_{Si} and LLI at all aging temperatures, while LAM_{Si} is more pronounced at higher temperatures due to higher cycle numbers. Still, LLI remained the dominant degradation mode at all temperatures. EIS analysis showed that for the cells aged at 10 °C and 25 °C the sudden drop of the SoH is accompanied by a simultaneous sudden increase of the ohmic, SEI, anode and diffusion resistance. Notably, no significant change of the cathode resistance was observed at the knee point. Coulombic efficiency analysis correlated the on-set of significant irreversible Li plating with the knee point at 10 °C and 25 °C. Post-mortem analysis provided additional insights into the sudden failure of the cells. Li plating was observed close to the cathode current collector tab at all temperatures, but only at 10 °C a significant amount of Li was plated on the core part of the anode sheet. The absence of a center pin led to significant deformation in the core part of the electrode sheets, resulting in inhomogeneous aging, particularly at 10 °C and 25 °C. The results suggest that optimizing the cell design with a tab-less configuration and incorporating a center pin could reduce inhomogeneous degradation in cylindrical cells, although this might come with certain drawbacks such as a reduced energy density.

Post-mortem analysis included SEM/EDS, XRD, and electrochemical tests to characterize the aging of the cells. Compared to the operando evaluation of the 21700 cell, the electrochemical tests in a three-electrode set-up provided a more accurate evaluation of LLI and LAM by measuring the residual capacities of the electrodes and performing DVA. For the cells aged at 25 °C and 35 °C, a more severe degradation of the cathode active material was detected than indicated by full-cell DVA, which was masked in the full cell by significant LLI.

The results of this study demonstrate that non-invasive diagnostic techniques such as dOCV, DVA and EIS are valuable tools for analyzing cell degradation particularly when combined, although their limitations should be considered during evaluation. Post-mortem analysis can offer deeper insights into the degradation mechanisms. However, it is often time-consuming, costly, and not always feasible. Future work should focus on further optimizing non-invasive diagnostic technique for more accurate degradation detection. In particular, advanced methods for plating detection, e.g. operando microscopy, and the coupling of degradation mechanisms with physical modeling have the potential to enhance the understanding of aging processes and how they are influenced by cell design and aging conditions.

CRediT authorship contribution statement

Christina Schmitt: Writing – review & editing, Writing – original draft, Visualization, Methodology, Investigation, Formal analysis, Conceptualization. **Dennis Kopljar:** Writing – review & editing, Supervision, Conceptualization. **K. Andreas Friedrich:** Writing – review & editing, Supervision.

Declaration of competing interest

The authors declare that they have no known competing financial interests or personal relationships that could have appeared to influence the work reported in this paper.

Acknowledgments

This work has been performed in the framework of the “FFAE” project at the German Aerospace Center (Deutsches Zentrum für Luft- und Raumfahrt, DLR). The authors would like to thank Ina Plock, Bhawna Rana and Giulia Bonfanti for the SEM/EDS measurements done within this study and Ruphay Frintrup and Mirjana Kugler for the

experimental support.

Appendix A. Supplementary data

Supplementary data to this article can be found online at https://doi.org/10.1016/j.est.2025.116486.

Data availability

Data will be made available on request.

References

[1] C. Schmitt, M. Gerle, D. Kopljar, K.A. Friedrich, Full parameterization study of a high-energy and high-power Li-ion cell for physicochemical models, J. Electrochem. Soc. 170 (7) (2023) 070509, https://doi.org/10.1149/1945-7111/ace1a7.

[2] C.R. Birkl, M.R. Roberts, E. McTurk, P.G. Bruce, D.A. Howey, Degradation diagnostics for lithium ion cells, J. Power Sources 341 (2017) 373–386, https://doi.org/10.1016/j.jpowsour.2016.12.011.

[3] T. Waldmann, A. Iturrondobeitia, M. Kasper, N. Ghanbari, F. Aguesse, E. Bekaert, L. Daniel, S. Genies, I.J. Gordon, M.W. Löble, E. De Vito, M. Wohlfahrt-Mehrens, Review - post-mortem analysis of aged lithium-ion batteries: disassembly methodology and physico-chemical analysis techniques, J. Electrochem. Soc. 163 (10) (2016) A2149–A2164, https://doi.org/10.1149/2.1211609jes.

[4] J.S. Edge, S. O'Kane, R. Prosser, N.D. Kirkaldy, A.N. Patel, A. Hales, A. Ghosh, W. Ai, J. Chen, J. Yang, S. Li, M.C. Pang, L. Bravo Diaz, A. Tomaszewska, M. W. Marzook, K.N. Radhakrishnan, H. Wang, Y. Patel, B. Wu, G.J. Offer, Lithium ion battery degradation: what you need to know, Phys. Chem. Chem. Phys. 23 (14) (2021) 8200–8221, https://doi.org/10.1039/d1cp00359c.

[5] M.M. Kabir, D.E. Demirocak, Degradation mechanisms in Li-ion batteries: a state-of-the-art review, Int. J. Energy Res. 41 (14) (2017) 1963–1986, https://doi.org/10.1002/er.3762.

[6] I. Bloom, A.N. Jansen, D.P. Abraham, J. Knuth, S.A. Jones, V.S. Battaglia, G. L. Henriksen, Differential voltage analyses of high-power, lithium-ion cells: 1. Technique and application, J. Power Sources 139 (1) (2005) 295–303, https://doi.org/10.1016/j.jpowsour.2004.07.021.

[7] P. Keil, A. Jossen, Calendar aging of NCA lithium-ion batteries investigated by differential voltage analysis and coulomb tracking, J. Electrochem. Soc. 164 (1) (2016) A6066–A6074, https://doi.org/10.1149/2.0091701jes.

[8] J. Schmitt, M. Schindler, A. Jossen, Change in the half-cell open-circuit potential curves of silicon–graphite and nickel-rich lithium nickel manganese cobalt oxide during cycle aging, J. Power Sources 506 (2021) 230240, https://doi.org/10.1016/j.jpowsour.2021.230240.

[9] J. Schmitt, M. Schindler, A. Oberbauer, A. Jossen, Determination of degradation modes of lithium-ion batteries considering aging-induced changes in the half-cell open-circuit potential curve of silicon–graphite, J. Power Sources 532 (2022) 231296, https://doi.org/10.1016/j.jpowsour.2022.231296.

[10] M. Dubarry, D. Anseán, Best practices for incremental capacity analysis, Front. Energy Res. 10 (2022), https://doi.org/10.3389/fenrg.2022.1023555.

[11] T.R. Tanim, M.G. Shirk, R.L. Bewley, E.J. Dufek, B.Y. Liaw, Fast charge implications: pack and cell analysis and comparison, J. Power Sources 381 (2018) 56–65, https://doi.org/10.1016/j.jpowsour.2018.01.091.

[12] A. Barai, K. Uddin, M. Dubarry, L. Somerville, A. McGordon, P. Jennings, I. Bloom, A comparison of methodologies for the non-invasive characterisation of commercial Li-ion cells, Prog. Energy Combust. Sci. 72 (2019) 1–31, https://doi.org/10.1016/j.pecs.2019.01.001.

[13] C. Heubner, T. Liebmann, O. Lohrberg, S. Cangaz, S. Maletti, A. Michaelis, Understanding component-specific contributions and internal dynamics in silicon/graphite blended electrodes for high-energy lithium-ion batteries, Batteries & Supercaps 5 (2021) e202100182, https://doi.org/10.1002/batt.202100182.

[14] T. Osaka, D. Mukoyama, H. Nara, Review - development of diagnostic process for commercially available batteries, especially lithium ion battery, by electrochemical impedance spectroscopy, J. Electrochem. Soc. 162 (14) (2015) A2529–A2537, https://doi.org/10.1149/2.0141514jes.

[15] P. Iurilli, C. Brivio, V. Wood, On the use of electrochemical impedance spectroscopy to characterize and model the aging phenomena of lithium-ion batteries: a critical review, J. Power Sources 505 (2021) 229860, https://doi.org/10.1016/j.jpowsour.2021.229860.

[16] C. Pastor-Fernández, K. Uddin, G.H. Chouchelamane, W.D. Widanage, J. Marco, A comparison between electrochemical impedance spectroscopy and incremental capacity-differential voltage as Li-ion diagnostic techniques to identify and quantify the effects of degradation modes within battery management systems, J. Power Sources 360 (2017) 301–318, https://doi.org/10.1016/j.jpowsour.2017.03.042.

[17] H. Sun, B. Jiang, H. You, B. Yang, X. Wang, X. Wei, H. Dai, Quantitative analysis of degradation modes of lithium-ion battery under different operating conditions, Energies 14 (2) (2021) 350, https://doi.org/10.3390/en14020350.

[18] W. Hu, Y. Peng, Y. Wei, Y. Yang, Application of electrochemical impedance spectroscopy to degradation and aging research of lithium-ion batteries, J. Phys. Chem. C 127 (9) (2023) 4465–4495, https://doi.org/10.1021/acs.jpcc.3c00033.

[19] P. Shafiei Sabet, G. Stahl, D.U. Sauer, Non-invasive investigation of predominant processes in the impedance spectra of high energy lithium-ion batteries with nickel–cobalt–aluminum cathodes, J. Power Sources 472 (2020) 228189, https://doi.org/10.1016/j.jpowsour.2020.228189.

[20] P. Shafiei Sabet, D.U. Sauer, Separation of predominant processes in electrochemical impedance spectra of lithium-ion batteries with nickel-manganese-cobalt cathodes, J. Power Sources 425 (2019) 121–129, https://doi.org/10.1016/j.jpowsour.2019.03.068.

[21] L. Wildfeuer, N. Wassiliadis, A. Karger, F. Bauer, M. Lienkamp, Teardown analysis and characterization of a commercial lithium-ion battery for advanced algorithms in battery electric vehicles, J. Energy Storage 48 (2022) 103909, https://doi.org/10.1016/j.est.2021.103909.

[22] J. Illig, J.P. Schmidt, M. Weiss, A. Weber, E. Ivers-Tiffée, Understanding the impedance spectrum of 18650 $LiFePO_4$-cells, J. Power Sources 239 (2013) 670–679, https://doi.org/10.1016/j.jpowsour.2012.12.020.

[23] P. Shafiei Sabet, A.J. Warnecke, F. Meier, H. Witzenhausen, E. Martinez-Laserna, D. U. Sauer, Non-invasive yet separate investigation of anode/cathode degradation of lithium-ion batteries (nickel–cobalt–manganese vs. graphite) due to accelerated aging, J. Power Sources 449 (2020) 227369, https://doi.org/10.1016/j.jpowsour.2019.227369.

[24] R. He, Y. He, W. Xie, B. Guo, S. Yang, Comparative analysis for commercial li-ion batteries degradation using the distribution of relaxation time method based on electrochemical impedance spectroscopy, Energy 263 (2023) 125972, https://doi.org/10.1016/j.energy.2022.125972.

[25] B. Stiaszny, J.C. Ziegler, E.E. Krauss, M.J. Zhang, J.P. Schmidt, E. Ivers-Tiffée, Electrochemical characterization and post-mortem analysis of aged $LiMn_2O_4$-NMC/graphite lithium ion batteries part II: calendar aging, J. Power Sources 258 (2014) 61–75, https://doi.org/10.1016/j.jpowsour.2014.02.019.

[26] R. Wittman, M. Dubarry, S. Ivanov, B.W. Juba, J. Romàn-Kustas, A. Fresquez, J. Langendorf, R. Grant, G. Taggart, B. Chalamala, Y. Preger, Characterization of cycle-aged commercial NMC and NCA lithium-ion cells: I. Temperature-dependent degradation, J. Electrochem. Soc. 170 (12) (2023) 120538, https://doi.org/10.1149/1945-7111/ad1450.

[27] T. Waldmann, M. Wilka, M. Kasper, M. Fleischhammer, M. Wohlfahrt-Mehrens, Temperature dependent ageing mechanisms in lithium-ion batteries - a post-mortem study, J. Power Sources 262 (2014) 129–135, https://doi.org/10.1016/j.jpowsour.2014.03.112.

[28] M. Storch, S.L. Hahn, J. Stadler, R. Swaminathan, D. Vrankovic, C. Krupp, R. Riedel, Post-mortem analysis of calendar aged large-format lithium-ion cells: investigation of the solid electrolyte interphase, J. Power Sources 443 (2019) 227243, https://doi.org/10.1016/j.jpowsour.2019.227243.

[29] M. Klett, R. Eriksson, J. Groot, P. Svens, K.C. Högström, R.W. Lindström, H. Berg, T. Gustafson, G. Lindbergh, K. Edström, Non-uniform aging of cycled commercial $LiFePO_4$//graphite cylindrical cells revealed by post-mortem analysis, J. Power Sources 257 (2014) 126–137, https://doi.org/10.1016/j.jpowsour.2014.01.105.

[30] B. Stiaszny, J.C. Ziegler, E.E. Krauss, J.P. Schmidt, E. Ivers-Tiffée, Electrochemical characterization and post-mortem analysis of aged $LiMn_2O_4$-$Li(N_{i0.5}Mn_{0.3}Co_{0.2})O_2$/graphite lithium ion batteries. Part I: cycle aging, J. Power Sources 251 (2014) 439–450, https://doi.org/10.1016/j.jpowsour.2013.11.080.

[31] Y. Kobayashi, T. Kobayashi, K. Shono, Y. Ohno, Y. Mita, H. Miyashiro, Decrease in capacity in Mn-based/graphite commercial lithium-ion batteries, J. Electrochem. Soc. 160 (8) (2013) A1181–A1186, https://doi.org/10.1149/2.071308jes.

[32] M. Kassem, C. Delacourt, Postmortem analysis of calendar-aged graphite/$LiFePO_4$ cells, J. Power Sources 235 (2013) 159–171, https://doi.org/10.1016/j.jpowsour.2013.01.147.

[33] F. Alcaide, G. Álvarez, E. Bekaert, F. Bonilla, E. Gucciardi, I. Urdampilleta, R. Vicedo, E. Ayerbe, Exploring the influence of temperature on anode degradation in cycling-aged commercial cylindrical graphite-Si|NCA cells, J. Electrochem. Soc. 170 (8) (2023) 080523, https://doi.org/10.1149/1945-7111/acf160.

[34] P. Heugel, W. Märkle, T. Deich, O. von Kessel, J. Tübke, Thickness change and jelly roll deformation and its impact on the aging and lifetime of commercial 18650 cylindrical Li-ion cells with silicon containing anodes and nickel-rich cathodes, J. Energy Storage 53 (2022) 105101, https://doi.org/10.1016/j.est.2022.105101.

[35] Y. Xia, J. Zheng, C. Wang, M. Gu, Designing principle for Ni-rich cathode materials with high energy density for practical applications, Nano Energy 49 (2018) 434–452, https://doi.org/10.1016/j.nanoen.2018.04.062.

[36] C. Liu, K. Qian, D. Lei, B. Li, F. Kang, Y.-B. He, Deterioration mechanism of $LiNi_{0.8}Co_{0.15}Al_{0.05}O_2$/graphite–$SiO_x$ power batteries under high temperature and discharge cycling conditions, J. Mater. Chem. A 6 (1) (2018) 65–72, https://doi.org/10.1039/c7ta08703a.

[37] W. Li, X. Liu, H. Celio, P. Smith, A. Dolocan, M. Chi, A. Manthiram, Mn versus Al in layered oxide cathodes in lithium-ion batteries: a comprehensive evaluation on long-term cyclability, Adv. Energy Mater. 8 (15) (2018), https://doi.org/10.1002/aenm.201703154.

[38] S. Watanabe, M. Kinoshita, T. Hosokawa, K. Morigaki, K. Nakura, Capacity fading of $LiAl_yNi_{1-x-y}Co_xO_2$ cathode for lithium-ion batteries during accelerated calendar and cycle life tests (effect of depth of discharge in charge–discharge cycling on the suppression of the micro-crack generation of $LiAl_yNi_{1-x-y}Co_xO_2$ particle), J. Power Sources 260 (2014) 50–56, https://doi.org/10.1016/j.jpowsour.2014.02.103.

[39] S. Watanabe, M. Kinoshita, T. Hosokawa, K. Morigaki, K. Nakura, Capacity fade of $LiAl_yNi_{1-x-y}Co_xO_2$ cathode for lithium-ion batteries during accelerated calendar and cycle life tests (surface analysis of $LiAl_yNi_{1-x-y}Co_xO_2$ cathode after cycle tests in restricted depth of discharge ranges), J. Power Sources 258 (2014) 210–217, https://doi.org/10.1016/j.jpowsour.2014.02.018.

[40] D. Ma, Z. Cao, A. Hu, Si-based anode materials for Li-ion batteries: a mini review, Nano-Micro Lett. 6 (4) (2014) 347–358, https://doi.org/10.1007/s40820-014-0008-2.

[41] P. Li, H. Kim, S.-T. Myung, Y.-K. Sun, Diverting exploration of silicon anode into practical way: a review focused on silicon-graphite composite for lithium ion batteries, Energy Stor. Mater. 35 (2021) 550–576, https://doi.org/10.1016/j.ensm.2020.11.028.

[42] O. von Kessel, A. Avdyli, D. Vrankovic, K.P. Birke, Swelling, pressure evolution and aging in high-silicon/graphite composite lithium-ion batteries, J. Power Sources 610 (2024) 234582, https://doi.org/10.1016/j.jpowsour.2024.234582.

[43] A. Zülke, Y. Li, P. Keil, R. Burrell, S. Belaisch, M. Nagarathinam, M.P. Mercer, H. E. Hoster, High-energy nickel-cobalt-aluminium oxide (NCA) cells on idle: anode-versus cathode-driven side reactions, Batteries Supercaps 4 (6) (2021) 934–947, https://doi.org/10.1002/batt.202100046.

[44] K. Richter, T. Waldmann, N. Paul, N. Jobst, R.G. Scurtu, M. Hofmann, R. Gilles, M. Wohlfahrt-Mehrens, Low-temperature charging and aging mechanisms of Si/C composite anodes in Li-ion batteries: an operando neutron scattering study, ChemSusChem 13 (3) (2020) 529–538, https://doi.org/10.1002/cssc.201903139.

[45] L.K. Willenberg, P. Dechent, G. Fuchs, D.U. Sauer, E. Figgemeier, High-precision monitoring of volume change of commercial lithium-ion batteries by using strain gauges, Sustainability 12 (2) (2020) 557, https://doi.org/10.3390/su12020557.

[46] L. Willenberg, P. Dechent, G. Fuchs, M. Teuber, M. Eckert, M. Graff, N. Kürten, D. U. Sauer, E. Figgemeier, The development of jelly roll deformation in 18650 lithium-ion batteries at low state of charge, J. Electrochem. Soc. 167 (12) (2020) 120502, https://doi.org/10.1149/1945-7111/aba96d.

[47] A. Aufschläger, A. Durdel, A. Jossen, Identifying the origin of inhomogeneous degradation and irreversible swelling inside cylindrical 21700 high-energy lithium-ion cells, J. Energy Storage 90 (2024) 111726, https://doi.org/10.1016/j.est.2024.111726.

[48] A. Mikheenkova, A.J. Smith, K.B. Frenander, Y. Tesfamhret, N.R. Chowdhury, C.-W. Tai, T. Thiringer, R.W. Lindström, M. Hahlin, M.J. Lacey, Ageing of high energy density automotive Li-ion batteries: the effect of temperature and state-of-charge, J. Electrochem. Soc. 170 (8) (2023) 080503, https://doi.org/10.1149/1945-7111/aceb8f.

[49] N.R. Chowdhury, A.J. Smith, K. Frenander, A. Mikheenkova, R.W. Lindström, T. Thiringer, Influence of state of charge window on the degradation of Tesla lithium-ion battery cells, J. Energy Storage 76 (2024) 110001, https://doi.org/10.1016/j.est.2023.110001.

[50] J. Zhu, Y. Wang, Y. Huang, R. Bhushan Gopaluni, Y. Cao, M. Heere, M. J. Muhlbauer, L. Mereacre, H. Dai, X. Liu, A. Senyshyn, X. Wei, M. Knapp, H. Ehrenberg, Data-driven capacity estimation of commercial lithium-ion batteries from voltage relaxation, Nat. Commun. 13 (1) (2022) 2261, https://doi.org/10.1038/s41467-022-29837-w.

[51] L. Wang, B. Zhang, J. Pang, Y. Liu, X. Wang, Z. Chang, S. Lu, Aging process analysis of $LiNi_{0.88}Co_{0.09}Al_{0.03}O_2$/graphite–$SiO_x$ pouch cell, Electrochim. Acta 286 (2018) 219–230, https://doi.org/10.1016/j.electacta.2018.07.224.

[52] X. Hu, S. Li, H. Peng, F. Sun, Charging time and loss optimization for LiNMC and $LiFePO_4$ batteries based on equivalent circuit models, J. Power Sources 239 (2013) 449–457, https://doi.org/10.1016/j.jpowsour.2013.03.157.

[53] M. Xu, R. Wang, P. Zhao, X. Wang, Fast charging optimization for lithium-ion batteries based on dynamic programming algorithm and electrochemical-thermal-capacity fade coupled model, J. Power Sources 438 (2019), https://doi.org/10.1016/j.jpowsour.2019.227015.

[54] J. Wallauer, RelaxIS 3 Impedance Spectrum Analysis, 3.0.21, rhd instruments GmbH & Co. KG, Darmstadt, Germany, 2013–2024.

[55] P.M. Attia, A. Bills, F.B. Planella, P. Dechent, G. dos Reis, M. Dubarry, P. Gasper, R. Gilchrist, S. Greenbank, D. Howey, O. Liu, E. Khoo, Y. Preger, A. Soni, S. Sripad, A.G. Stefanopoulou, V. Sulzer, Review-"knees" in lithium-ion battery aging trajectories, J. Electrochem. Soc. 169 (6) (2022) 060517, https://doi.org/10.1149/1945-7111/ac6d13.

[56] K.P.C. Yao, J.S. Okasinski, K. Kalaga, J.D. Almer, D.P. Abraham, Operando quantification of (de)lithiation behavior of silicon-graphite blended electrodes for lithium-ion batteries, Adv. Energy Mater. 9 (2019) 1803380, https://doi.org/10.1002/aenm.201803380.

[57] J.R. Dahn, Phase diagram of Li_xC_6, Phys. Rev. B 44 (1991) 9170–9177, https://doi.org/10.1103/PhysRevB.44.9170.

[58] C. Didier, W.K. Pang, Z. Guo, S. Schmid, V.K. Peterson, Phase evolution and intermittent disorder in electrochemically lithiated graphite determined using in operando neutron diffraction, Chem. Mater. 32 (6) (2020) 2518–2531, https://doi.org/10.1021/acs.chemmater.9b05145.

[59] C. Schmitt, A. Kube, N. Wagner, K.A. Friedrich, Understanding the influence of temperature on phase evolution during lithium-graphite (de-)intercalation processes: an operando X-ray diffraction study, ChemElectroChem 9 (2022) 43–51, https://doi.org/10.1002/celc.202101342.

[60] A.Y.R. Prado, M.-T.F. Rodrigues, S.E. Trask, L. Shaw, D.P. Abraham, Electrochemical dilatometry of Si-bearing electrodes: dimensional changes and experiment design, J. Electrochem. Soc. 167 (16) (2020) 160551, https://doi.org/10.1149/1945-7111/abd465.

[61] M. Lewerenz, A. Marongiu, A. Warnecke, D.U. Sauer, Differential voltage analysis as a tool for analyzing inhomogeneous aging: a case study for $LiFePO_4$|graphite cylindrical cells, J. Power Sources 368 (2017) 57–67, https://doi.org/10.1016/j.jpowsour.2017.09.059.

[62] J. Zhu, M.S. Dewi Darma, M. Knapp, D.R. Sørensen, M. Heere, Q. Fang, X. Wang, H. Dai, L. Mereacre, A. Senyshyn, X. Wei, H. Ehrenberg, Investigation of lithium-ion battery degradation mechanisms by combining differential voltage analysis and alternating current impedance, J. Power Sources 448 (2020) 227575, https://doi.org/10.1016/j.jpowsour.2019.227575.

[63] J.P. Fath, D. Dragicevic, L. Bittel, A. Nuhic, J. Sieg, S. Hahn, L. Alsheimer, B. Spier, T. Wetzel, Quantification of aging mechanisms and inhomogeneity in cycled lithium-ion cells by differential voltage analysis, J. Energy Storage 25 (2019) 100813, https://doi.org/10.1016/j.est.2019.100813.

[64] Y.-C. Chang, H.-J. Sohn, Electrochemical impedance analysis for lithium ion intercalation into graphitized carbons, J. Electrochem. Soc. 147 (1) (2000) 50–58, https://doi.org/10.1149/1.1393156.

[65] P.-C. Tsai, B. Wen, M. Wolfman, M.-J. Choe, M.S. Pan, L. Su, K. Thornton, J. Cabana, Y.-M. Chiang, Single-particle measurements of electrochemical kinetics in NMC and NCA cathodes for Li-ion batteries, Energ. Environ. Sci. 11 (4) (2018) 860–871, https://doi.org/10.1039/c8ee00001h.

[66] J. Zhu, M. Knapp, X. Liu, P. Yan, H. Dai, X. Wei, H. Ehrenberg, Low-temperature separating lithium-ion battery interfacial polarization based on distribution of relaxation times (DRT) of impedance, IEEE Trans. Transp. Electrif. 7 (2) (2021) 410–421, https://doi.org/10.1109/tte.2020.3028475.

[67] M. Steinhauer, S. Risse, N. Wagner, K.A. Friedrich, Investigation of the solid electrolyte interphase formation at graphite anodes in lithium-ion batteries with electrochemical impedance spectroscopy, Electrochim. Acta 228 (2017) 652–658, https://doi.org/10.1016/j.electacta.2017.01.128.

[68] D. Andre, M. Meiler, K. Steiner, C. Wimmer, T. Soczka-Guth, D.U. Sauer, Characterization of high-power lithium-ion batteries by electrochemical impedance spectroscopy. I. Experimental investigation, J. Power Sources 196 (12) (2011) 5334–5341, https://doi.org/10.1016/j.jpowsour.2010.12.102.

[69] A. Maheshwari, M. Heck, M. Santarelli, Cycle aging studies of lithium nickel manganese cobalt oxide-based batteries using electrochemical impedance spectroscopy, Electrochim. Acta 273 (2018) 335–348, https://doi.org/10.1016/j.electacta.2018.04.045.

[70] J. Sturm, A. Frank, A. Rheinfeld, S.V. Erhard, A. Jossen, Impact of electrode and cell design on fast charging capabilities of cylindrical lithium-ion batteries, J. Electrochem. Soc. 167 (13) (2020) 130505, https://doi.org/10.1149/1945-7111/abb40c.

[71] E. Teliz, C.F. Zinola, V. Díaz, Identification and quantification of ageing mechanisms in Li-ion batteries by electrochemical impedance spectroscopy, Electrochim. Acta 426 (2022) 140801, https://doi.org/10.1016/j.electacta.2022.140801.

[72] P. Gargh, A. Sarkar, Y.H. Lui, S. Shen, C. Hu, S. Hu, I.C. Nlebedim, P. Shrotriya, Correlating capacity fade with film resistance loss in fast charging of lithium-ion battery, J. Power Sources 485 (2021) 229360, https://doi.org/10.1016/j.jpowsour.2020.229360.

[73] X. Chen, L. Li, M. Liu, T. Huang, A. Yu, Detection of lithium plating in lithium-ion batteries by distribution of relaxation times, J. Power Sources 496 (2021) 229867, https://doi.org/10.1016/j.jpowsour.2021.229867.

[74] S. Schindler, M. Bauer, M. Petzl, M.A. Danzer, Voltage relaxation and impedance spectroscopy as in-operando methods for the detection of lithium plating on graphitic anodes in commercial lithium-ion cells, J. Power Sources 304 (2016) 170–180, https://doi.org/10.1016/j.jpowsour.2015.11.044.

[75] A. Raj, M.-T.F. Rodrigues, D.P. Abraham, Rate-dependent aging resulting from fast charging of Li-ion cells, J. Electrochem. Soc. 167 (12) (2020) 120517, https://doi.org/10.1149/1945-7111/abace9.

[76] J. Fan, S. Tan, Studies on charging lithium-ion cells at low temperatures, J. Electrochem. Soc. 153 (6) (2006) A1081–A1092, https://doi.org/10.1149/1.2190029.

[77] B.V. Ratnakumar, M.C. Smart, Lithium plating behavior in lithium-ion cells, ECS Trans. 25 (36) (2010) 241–252, https://doi.org/10.1149/1.3393860.

[78] M. Petzl, M.A. Danzer, Nondestructive detection, characterization, and quantification of lithium plating in commercial lithium-ion batteries, J. Power Sources 254 (2014) 80–87, https://doi.org/10.1016/j.jpowsour.2013.12.060.

[79] M.C. Smart, B.V. Ratnakumar, Effects of electrolyte composition on lithium plating in lithium-ion cells, J. Electrochem. Soc. 158 (4) (2011) A379–A389, https://doi.org/10.1149/1.3544439.

[80] C. Uhlmann, J. Illig, M. Ender, R. Schuster, E. Ivers-Tiffée, In situ detection of lithium metal plating on graphite in experimental cells, J. Power Sources 279 (2015) 428–438, https://doi.org/10.1016/j.jpowsour.2015.01.046.

[81] C. von Lüders, V. Zinth, S.V. Erhard, P.J. Osswald, M. Hofmann, R. Gilles, A. Jossen, Lithium plating in lithium-ion batteries investigated by voltage relaxation and in situ neutron diffraction, J. Power Sources 342 (2017) 17–23, https://doi.org/10.1016/j.jpowsour.2016.12.032.

[82] Z.M. Konz, E.J. McShane, B.D. McCloskey, Detecting the onset of lithium plating and monitoring fast charging performance with voltage relaxation, ACS Energy Lett. 5 (6) (2020) 1750–1757, https://doi.org/10.1021/acsenergylett.0c00831.

[83] X.-G. Yang, S. Ge, T. Liu, Y. Leng, C.-Y. Wang, A look into the voltage plateau signal for detection and quantification of lithium plating in lithium-ion cells, J. Power Sources 395 (2018) 251–261, https://doi.org/10.1016/j.jpowsour.2018.05.073.

[84] M. Bauer, B. Rieger, S. Schindler, P. Keil, M. Wachtler, M.A. Danzer, A. Jossen, Multi-phase formation induced by kinetic limitations in graphite-based lithium-ion cells: analyzing the effects on dilation and voltage response, J. Energy Storage 10 (2017) 1–10, https://doi.org/10.1016/j.est.2016.11.006.

[85] W. Mei, Y. Zhang, Y. Li, P. Zhuo, Y. Chu, Y. Chen, L. Jiang, H. Zhou, J. Sun, Q. Wang, Unveiling voltage evolution during Li plating-relaxation-Li stripping cycling of lithium-ion batteries, Energy Stor. Mater. 66 (2024) 103193, https://doi.org/10.1016/j.ensm.2024.103193.

[86] A. Pfrang, A. Kersys, A. Kriston, D.U. Sauer, C. Rahe, S. Käbitz, E. Figgemeier, Long-term cycling induced jelly roll deformation in commercial 18650 cells, J. Power Sources 392 (2018) 168–175, https://doi.org/10.1016/j.jpowsour.2018.03.065.

[87] W. Ai, N. Kirkaldy, Y. Jiang, G. Offer, H. Wang, B. Wu, A composite electrode model for lithium-ion batteries with silicon/graphite negative electrodes, J. Power Sources 527 (2022) 231142, https://doi.org/10.1016/j.jpowsour.2022.231142.
[88] S.J. Harris, A. Timmons, D.R. Baker, C. Monroe, Direct in situ measurements of Li transport in Li-ion battery negative electrodes, Chem. Phys. Lett. 485 (4) (2010) 265–274, https://doi.org/10.1016/j.cplett.2009.12.033.
[89] A.J. Smith, Y. Fang, A. Mikheenkova, H. Ekström, P. Svens, I. Ahmed, M.J. Lacey, G. Lindbergh, I. Furó, R.W. Lindström, Localized lithium plating under mild cycling conditions in high-energy lithium-ion batteries, J. Power Sources 573 (2023) 233118, https://doi.org/10.1016/j.jpowsour.2023.233118.
[90] Y. Qiu, X. Zhang, C. Usubelli, D. Mayer, C. Linder, J. Christensen, Understanding thermal and mechanical effects on lithium plating in lithium-ion batteries, J. Power Sources 541 (2022) 231632, https://doi.org/10.1016/j.jpowsour.2022.231632.
[91] M. Broussely, P. Biensan, F. Bonhomme, P. Blanchard, S. Herreyre, K. Nechev, R. J. Staniewicz, Main aging mechanisms in Li ion batteries, J. Power Sources 146 (1) (2005) 90–96, https://doi.org/10.1016/j.jpowsour.2005.03.172.
[92] L. Boveleth, A. Lindner, W. Menesklou, T. Danner, A. Latz, Material parameters affecting Li plating in Si/graphite composite electrodes, Electrochim. Acta 506 (2024) 145010, https://doi.org/10.1016/j.electacta.2024.145010.
[93] L. David, D. Mohanty, L. Geng, R.E. Ruther, A.S. Sefat, E. Cakmak, G.M. Veith, H. M. Meyer, H. Wang, D.L. Wood, High-voltage performance of Ni-rich NCA cathodes: linking operating voltage with cathode degradation, ChemElectroChem 6 (22) (2019) 5571–5580, https://doi.org/10.1002/celc.201901338.
[94] G.W. Nam, N.-Y. Park, K.-J. Park, J. Yang, J. Liu, C.S. Yoon, Y.-K. Sun, Capacity fading of Ni-rich NCA cathodes: effect of microcracking extent, ACS Energy Lett. 4 (12) (2019) 2995–3001, https://doi.org/10.1021/acsenergylett.9b02302.
[95] J. Sieg, J. Bandlow, T. Mitsch, D. Dragicevic, T. Materna, B. Spier, H. Witzenhausen, M. Ecker, D.U. Sauer, Fast charging of an electric vehicle lithium-ion battery at the limit of the lithium deposition process, J. Power Sources 427 (2019) 260–270, https://doi.org/10.1016/j.jpowsour.2019.04.047.